FAST CALIBRATION AND IMAGE RECONSTRUCTION FOR MAGNETIC PARTICLE IMAGING

A THESIS SUBMITTED TO

THE GRADUATE SCHOOL OF ENGINEERING AND SCIENCE

OF BILKENT UNIVERSITY

IN PARTIAL FULFILLMENT OF THE REQUIREMENTS FOR

THE DEGREE OF

MASTER OF SCIENCE

IN

ELECTRICAL AND ELECTRONICS ENGINEERING

By

Serhat İlbey

May 2018

FAST CALIBRATION AND IMAGE RECONSTRUCTION FOR MAGNETIC PARTICLE IMAGING
By Serhat İlbey
May 2018

We certify that we have read this thesis and that in our opinion it is fully adequate, in scope and in quality, as a thesis for the degree of Master of Science.

Emine Ülkü Sarıtaş Çukur (Advisor)

Can Barış Top (Co-Advisor)

Tolga Çukur

Nevzat Güneri Gençer

Approved for the Graduate School of Engineering and Science:

Ezhan Karaşan
Director of the Graduate School

ABSTRACT

FAST CALIBRATION AND IMAGE RECONSTRUCTION FOR MAGNETIC PARTICLE IMAGING

Serhat İlbey
M.S. in Electrical and Electronics Engineering
Advisor: Emine Ülkü Sarıtaş Çukur
Co-Advisor: Can Barış Top
May 2018

Magnetic particle imaging (MPI) is a relatively new medical imaging modality that images the spatial distribution of magnetic nanoparticles (MNPs) administered to the body. For image reconstruction with the system matrix (SM) approach, a time-consuming calibration scan is necessary, in which a single MNP sample is placed and scanned inside the full field-of-view (FOV). Moreover, for a relatively large 3D high-resolution FOV, the reconstructed SM is too large to get high quality images in real-time using the standard state-of-the-art techniques. In this thesis, for the calibration scan, the use of coded calibration scenes (CCSs) is proposed, which utilizes MNP samples at multiple positions inside the FOV. The SM, which is sparse in the discrete cosine transform domain, is reconstructed using the Alternating Direction Method of Multipliers (ADMM) with l_1-norm minimization. The effectiveness of the CCSs for different parameter sets is analyzed via simulations, and the results are compared with the standard sparse reconstruction technique. As the MPI images are naturally sparse, ADMM is also proposed for image reconstruction, minimizing the total variation and l_1-norm. Image quality is compared with the images obtained by widely used MPI image reconstruction algorithms: Algebraic Reconstruction Technique, Nonnegative Fused LASSO, and X-space-based projection reconstruction. Moreover, ADMM is parallelized on a GPU for real-time image reconstruction. The results show that the required number of measurements for system calibration is substantially reduced with the proposed methods, and the reconstruction performance is significantly improved in terms of both image quality and speed.

Keywords: magnetic particle imaging, compressed sensing, system matrix, image reconstruction.

ÖZET

MANYETİK PARÇACIK GÖRÜNTÜLEME İÇİN HIZLI KALİBRASYON VE GÖRÜNTÜ GERİÇATIMI

Serhat İlbey
Elektrik ve Elektronik Mühendisliği, Yüksek Lisans
Tez Danışmanı: Emine Ülkü Sarıtaş Çukur
İkinci Tez Danışmanı: Can Barış Top
Mayıs 2018

Manyetik parçacık görüntüleme (MPG), vücuda enjekte edilen manyetik nanoparçacıkların (MNP) uzamsal dağılımını görüntülemede kullanılan görece yeni bir tıbbi görüntüleme yöntemidir. Sistem matrisi (SM) yaklaşımı ile yapılan görüntü geriçatımında, tek bir MNP örneğinin tüm görüş alanı (GA) içine yerleştirilmesi ve taranması yoluyla yapılan ve uzun zaman süren bir kalibrasyon taramasına ihtiyaç vardır. Üstelik SM'nin boyutu, 3B yüksek çözünürlüklü ve görece geniş GA için standart geriçatım teknikleri ile gerçek zamanda yüksek kaliteli görüntüler elde edilemeyecek kadar büyüktür. Bu tezde, kalibrasyon taraması için GA'da birçok pozisyonda MNP örnekleri içeren kodlu kalibrasyon sahneleri (KKS) önerilmektedir. Ayrık kosinüs dönüşümü uzayında seyrek olan SM, l_1-norm minimizasyonu ile Yön Değiştiren Çarpanlar Yöntemi (YDÇY) kullanılarak geriçatılmıştır. KKS'lerin etkinliği, farklı parametre kümelerinde benzetimler yoluyla analiz edilmiş ve sonuçlar standart seyrek geriçatım tekniği ile karşılaştırılmıştır. MPG görüntüleri doğal olarak seyrek oldukları için, YDÇY'nin toplam değişinti ve l_1-normu birlikte minimize eden versiyonu, görüntü geriçatımı için de önerilmiştir. Görüntü kalitesi MPG görüntü geriçatımında çokça kullanılan şu algoritmaların sonuçları ile karşılaştırılmıştır: Cebirsel geriçatım tekniği, negatif olmayan kaynaşık LASSO ve X-uzayı tabanlı izdüşüm yöntemi. Dahası, YDÇY gerçek zamanlı görüntü geriçatımı için GPU üzerinde paralellenmiştir. Önerilen yöntemler kullanılarak elde edilen sonuçlara göre, sistem kalibrasyonu için gerekli ölçüm süresi büyük ölçüde azaltılmış, ve görüntü kalitesi ve hız açısından görüntü geriçatım performansı önemli oranda iyileştirilmiştir.

Anahtar sözcükler: manyetik parçacık görüntüleme, sıkıştırılmış algılama, sistem matrisi, görüntü geriçatımı.

Acknowledgement

First of all, I would like to thank my supervisors, Dr. Can Barış Top and Asst. Prof. Dr. Emine Ülkü Sarıtaş for their valuable advices and excellent support during my thesis work.

Besides my advisors, I also would like to thank to my thesis committee: Asst. Prof. Dr. Tolga Çukur and Prof. Dr. Nevzat Güneri Gençer for their insightful comments and critical questions.

Next comes my colleagues Dr. H. Emre Güven, Mert Kalfa, Dr. Emre Kopanoğlu, and Oğuzhan Fatih Kar in Advanced Sensing Research Program Department, ASELSAN Research Center, for their support and readiness to help during my thesis work. I also would like to thank to my colleague Alper Güngör for providing the MATLAB and CUDA implementation of the ADMM algorithm that I used in this thesis work and fruitful discussions.

Last, but not least, I would like to thank my dear wife Merve for her great support, understanding, and love.

This work was supported by the Scientific and Technological Research Council of Turkey (TÜBİTAK, Project numbers: 9050103 and 115E677).

Contents

List of Figures

List of Tables

Chapter 1

Introduction

Magnetic Particle Imaging (MPI) is a relatively new imaging modality in which magnetic nanoparticles (MNPs) are introduced inside the body, and their spatial distribution (i.e., density) is imaged [1]. The applications of MPI include but are not limited to angiography, stem cell tracking, and tumor imaging [2]. In MPI, a static magnetic field called the selection field (SF) is used to create a field free region (FFR). This magnetic field can be generated using a pair of coils with opposite polarities. The MNPs inside the FFR respond to an alternating magnetic field called the drive field (DF) by changing their magnetization direction via Brownian and Néel relaxation mechanisms. Outside the FFR, the MNPs are saturated with negligible response to the applied DF. Since the magnetization curve of the MNPs is nonlinear, the nanoparticles within the FFR yield a magnetization response that contains the harmonics of the applied DF frequency. This response is detected via receive coils. The induced signal amplitude depends on the number of MNPs inside the FFR. The FFR is then swept through the entire imaging volume to generate a three-dimensional (3D) image. The resolution of this image depends on the magnetic field gradient in the FFR, the magnetization and environmental properties of the MNPs, and the signal-to-noise ratio (SNR) of the received signal [3, 4].

MPI images can be reconstructed either using a system matrix (SM) approach

that involves a separate calibration procedure [1, 5], or alternatively in the image domain (i.e., x-space) based on several assumptions on the MNP properties and the magnetic fields [6]. In the calibration procedure of the SM method, a small MNP sample is placed at a specific voxel location while the entire field-of-view (FOV) is scanned. This procedure is repeated for all voxel locations within the FOV. The responses measured at each voxel location are then saved as the SM. Next, the actual object of interest is imaged, and a linear system of equations (LSE) is formed using the SM and the response of the object. The unknown MNP distribution for the object of interest is reconstructed by solving this LSE. Typically, this inverse problem is solved via iterative regularized methods such as the Kaczmarz method, also known as the Algebraic Reconstruction Technique (ART) [5]. Recently, the Nonnegative Fused LASSO (NFL) method, which minimizes the total variation (TV) and l_1-norm solution, is reported to perform better for preserving edge discontinuities in the image [7].

The drawback of the SM method is the long measurement times of the calibration process, which takes hours for even a small FOV [8] of size 32 mm x 32 mm x 32 mm. To mitigate this problem, compressed sensing (CS) methods were proposed for SM measurement and reconstruction. The rows of the SM, i.e., the spatial sensitivity distribution of the imaging system, can be represented with a much smaller number of elements compared to the grid size of the image in the discrete cosine transform (DCT) or discrete Chebyshev transform (DChT) domains [9]. Therefore, the SM can be reconstructed with smaller number of measurements at randomly selected calibration positions inside the FOV. Acceptable degradation on the MPI images can be achieved using only $10\% - 20\%$ of the full grid for the calibration [10]. This rate can be further decreased by using the symmetry of the SM rows [11]. Although these procedures accelerate the calibration process, calibration durations may still be a problem for large FOVs needed in clinical scans.

In MPI, the FFR is typically characterized as a small ellipsoidal volume, which is called a Field Free Point (FFP) [1]. As the received signal is directly related to the number of particles in the FFR, the field free line (FFL) imaging has been proposed to increase the sensitivity via using a larger FFR volume [12]. The

conventional reconstruction method in FFL MPI is based on projection imaging, which uses the time-domain data to perform the reconstruction in the image domain [13–15].

There are three main contributions of this thesis study in the field of MPI. Firstly, the projection-based x-space and SM reconstruction techniques for an FFL-MPI system is compared, in terms of both reconstruction time and image quality [16, 17]. For the SM reconstruction, the use of an Alternating Direction Method of Multipliers (ADMM) algorithm is proposed, which is based on an Augmented Lagrangian Method [18]. ADMM is a recently re-invented technique that solves a given problem by dividing it into smaller sub-problems using a quasi-Newton approach. Moreover, the algorithm includes augmented Lagrangian terms that yield a fast convergence speed. The SM-based NFL algorithm is also implemented, and the results are compared with those of the proposed ADMM approach.

Secondly, ADMM is implemented on CUDA environment and real-time 3D image reconstruction results are presented on an NVIDIA® GeForce® GTX 1080 graphical processing unit (GPU). The speed performance of these results were compared with those obtained with a workstation having Intel® Xeon® E5-2637 v4 @ 3.50 GHz (x2) central processing units (CPUs) and 256 GB random access memory (RAM).

Finally, in this thesis, the use of coded calibration scenes (CCSs) is proposed to decrease the number of measurements in the calibration process [19]. Rather than scanning a single MNP sample at different positions, a number of coded scenes, each of which includes multiple MNP samples at random positions were used. In the calibration procedure, the scenes were imaged, and then the SM was reconstructed using these measurements with ADMM. The effect of the number of scenes on the quality of the reconstructed images were analysed using simulations. The results were also compared with those obtained from the standard single-MNP sparse scanning method in [10]. Instead of using multiple CCSs, rotating and/or sliding CCSs are also proposed for the system calibration. It is shown that the SM reconstructed via CCSs yields significantly better image quality

with respect to the standard sparse SM reconstruction method using single-MNP measurements.

This thesis is organized as follows: In Chapter 2, the principles of MPI is presented. The MPI signal equation is derived, and the image reconstruction methods and the sparsity property of the SM are shown. In Chapter 3, ADMM is proposed as a fast image reconstruction algorithm for MPI. Then, the image reconstruction algorithms in MPI are comparatively analyzed. The GPU performance of ADMM is presented for 3D real-time image reconstruction. The GPU implementation is compared to CPU implementation of ADMM in terms of reconstruction speed. In Chapter 4, the CCS approach for system calibration is presented and the results are compared with the standard sparse reconstruction method. In Chapter 5, the conclusions for the presented works are given.

Chapter 2

Principles of Magnetic Particle Imaging

2.1 Signal Equation

In MPI, a static magnetic field gradient with an FFR is generated in the FOV. The MNPs inside this FFR are excited by a time-varying magnetic field and the signal due to the time-varying MNP magnetization is received by the receive coils. The magnetization of the MNPs that are outside of the FFR are saturated, so that they do no induce any signal [1].

For the 1-dimensional (1D) case, assume that the MPI system has a static magnetic field gradient $-G$ $[A/m^2]$ and a time-varying magnetic field $H_0(t)$ $[A/m]$ is applied in addition [20]. The static magnetic field can be realized by a Maxwell coil topology, as shown in Fig. 2.1. If the value of the static magnetic field at the origin is zero, then the total magnetic field as a function of x is:

$$H(x,t) = H_0(t) - Gx. \tag{2.1}$$

Spatial encoding in MPI can be done by scanning an FFP in the FOV. So, the

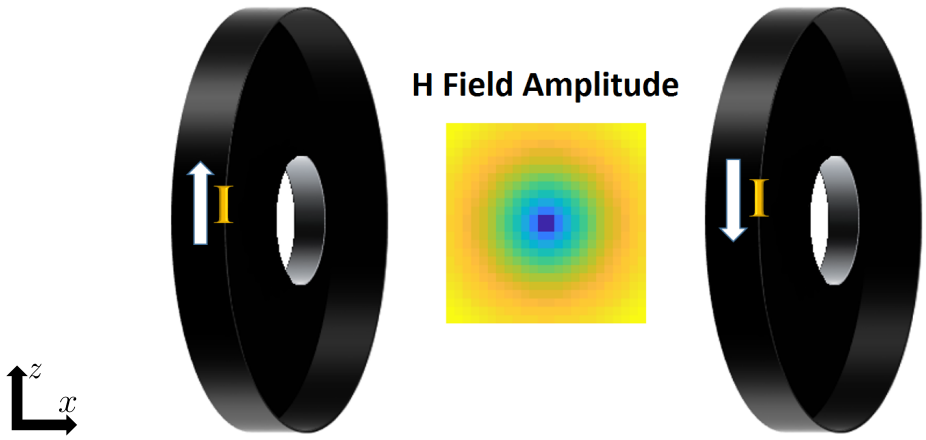

Figure 2.1: Maxwell coil pair to generate a FFP (blue region) in the FOV.

location of the FFP can be calculated from $H(x,t) = 0$. Hence,

$$x_s(t) = G^{-1}H_0(t). \tag{2.2}$$

If we substitute $x_s(t)$ to Eqn. 2.1, the position- and time-dependent magnetic field can also be expressed as:

$$H(x,t) = G(x_s(t) - x). \tag{2.3}$$

The magnetization of the MNPs in response to an applied external magnetic field can be described by the equation

$$M(H) = mc\mathcal{L}[kH], \tag{2.4}$$

where m $[Am^2]$ is the magnetic moment of the MNPs, H $[A/m]$ is the magnetic field applied, c $[m^{-3}]$ is the particle density, and $\mathcal{L}$ is the Langevin function that models the magnetization of MNPs (see Fig. 2.2):

$$\mathcal{L}[kH] = coth(kH) - \frac{1}{kH}, \tag{2.5}$$

where k is a property of the MNPs [20], which is

$$k = \frac{\mu_0 m}{k_B T}, \tag{2.6}$$

where k_B is the Boltzmann's constant, T is the absolute temperature, and μ_0 is the vacuum permeability.

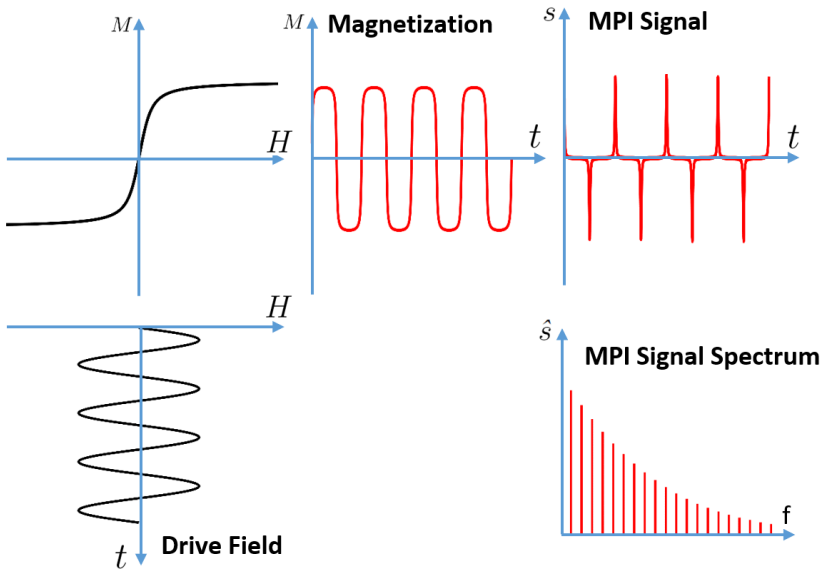

a)

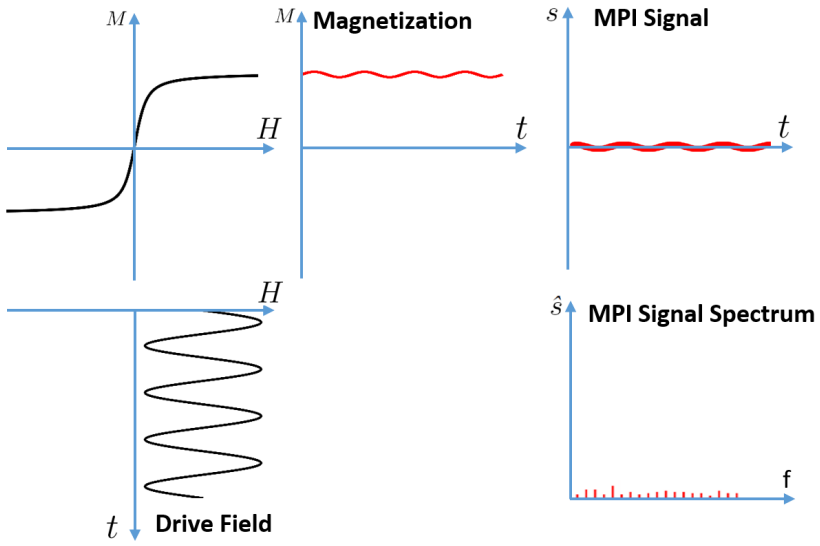

b)

Figure 2.2: MPI signal encoding for the cases **a)** the MNP sample is in the FFP and **b)** the MNP sample is outside of the FFP, with its magnetization saturated. The MPI signal, which is proportional to the time derivative of the magnetization, is given on the right side of the figures, together with its spectrum.

For the 1D case of MNP density along the x axis, $c(x,y,z) \triangleq c(x)\delta(y)\delta(z)$, the magnetization becomes:

$$M(x,t) = mc(x)\delta(y)\delta(z)\mathcal{L}[kG(x_s(t)-x)]. \tag{2.7}$$

Hence, the 1D magnetization flux, Φ, as a function of time is:

$$\begin{aligned}\Phi(t) &= -m\int\int\int c(u)\delta(v)\delta(w)\mathcal{L}[kG(x_s(t)-u)]dudvdw \\ &= -mc(x) * \mathcal{L}[kGx]\Big|_{x=x_s(t)}\end{aligned} \tag{2.8}$$

The 1D MPI signal can then be written as [20]:

$$s(t) = \sigma_x\frac{d\Phi}{dt} = \sigma_x mc(x) * \dot{\mathcal{L}}[kGx]\Big|_{x=x_s(t)} kG\dot{x}_s(t), \tag{2.9}$$

where σ_x is the sensitivity of the receive coil, which is assumed to be uniform in space.

A similar derivation can be performed for the 3D MPI signal. While the steps are more complicated, after several assumptions, the 3D MPI signal can be written as [6]:

$$s(t) = \sigma(\mathbf{x})mc(\mathbf{x}) * * * \frac{\|\dot{\mathbf{x}}_s\|}{H_{sat}}\mathbf{h}(\mathbf{x})\hat{\dot{\mathbf{x}}}_s\Big|_{\mathbf{x}=\mathbf{x}_s(t)}, \tag{2.10}$$

where $\mathbf{x}$ is the 3D location in the FOV, H_{sat} is the magnetic field required for saturation, $\dot{\mathbf{x}}_s$ is the time derivative of $\mathbf{x}_s$, $\mathbf{h}(\mathbf{x})$ is the 3D point spread function (PSF) of the MPI system given as

$$\begin{aligned}\mathbf{h}(\mathbf{x}) = \dot{\mathcal{L}}[\|\mathbf{Gx}\|/H_{sat}]\frac{\mathbf{Gx}}{\|\mathbf{Gx}\|}\left(\frac{\mathbf{Gx}}{\|\mathbf{Gx}\|}\right)^T\mathbf{G} + \\ \frac{\mathcal{L}[\|\mathbf{Gx}\|/H_{sat}]}{\|\mathbf{Gx}\|/H_{sat}}\left(\mathbf{I}-\frac{\mathbf{Gx}}{\|\mathbf{Gx}\|}\left(\frac{\mathbf{Gx}}{\|\mathbf{Gx}\|}\right)^T\right)\mathbf{G},\end{aligned} \tag{2.11}$$

where $\mathbf{G}$ is the 3D magnetic field gradient matrix, and $\mathbf{I}$ is the 3 x 3 identity matrix.

To scan the FFP across all the positions inside the FOV, several different trajectories have been proposed [21]. In this thesis, in the simulations featuring an FFP MPI system, the Lissajous trajectory is used (see Fig. 2.3) as it outperforms other trajectories such as the Cartesian and the spiral in terms of image quality [21].

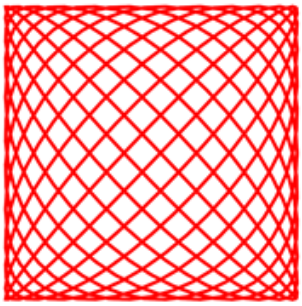

Figure 2.3: The Lissajous trajectory, which is commonly used for scanning a FFP across the FOV.

2.2 Image Reconstruction Approaches

MPI images can be reconstructed either using a SM approach that involves a separate calibration procedure [1], or alternatively, using the x-space method, based on several assumptions on the MNP properties and the magnetic fields [20].

2.2.1 X-Space Reconstruction Method

In the x-space approach, the received MPI signal given in Eqn. 2.9 is processed with simple velocity compensation and gridding steps to convert it into the so-called x-space domain. We can express the x-space 1D image equation, as following [20]:

$$\mathrm{IMG}(x_s(t)) = \frac{s(t)}{\sigma_x mkG\dot{x}_s(t)} = c(x) * \dot{\mathcal{L}}[kGx]\Big|_{x=x_s(t)}. \tag{2.12}$$

Here, the derivative of the Langevin function corresponds to the 1D PSF. Similarly, the 3D image equation can be shown to be equal to [6]:

$$\mathrm{IMG}(\mathbf{x}_s(t)) = c(\mathbf{x}) * * * \hat{\dot{\mathbf{x}}}_s \cdot \mathbf{h}(\mathbf{x})\hat{\dot{\mathbf{x}}}_s\Big|_{x=x_s(t)}. \tag{2.13}$$

2.2.1.1 Projection based X-Space Reconstruction for FFL MPI Systems

An FFL instead of an FFP can be used to increase the sensitivity of the MPI system [12]. For 3D imaging with this approach, the FFL is rotated and translated to cover the entire FOV. For this approach, the MPI signal equation at projection angle θ_k can be reformulated as follows:

$$S_r(\theta_k, t) = \left(D\Lambda'(t)(\hat{m}(\nu) * R(\mathbf{c})(\theta_k, \nu))\right), \tag{2.14}$$

where ν is the distance of the FFL to the center of the FOV given as

$$\nu(t) = \frac{D}{G}\Lambda(t), \tag{2.15}$$

$\hat{m}(\nu)$ is the convolution kernel given as

$$\hat{m}(v) = m\frac{d}{d\nu}\mathcal{L}\left(\frac{\mu_0 G\nu m}{k_B T}\right), \tag{2.16}$$

D is the amplitude of the DF, $\Lambda(t) = sin(2\pi f_0 t)$ is the excitation function of the DF, f_0 is the DF frequency, and $R(\mathbf{c})$ is the Radon transform of the particle density [15].

For the reconstruction process, the time domain signal is divided by the FFL velocity, and transformed to the spatial domain using interpolation. Next, the signal is deconvolved with the convolution kernel ($\hat{m}$). This process is repeated for all rotation angles. Finally, the image is reconstructed with inverse Radon transform [13, 15].

2.2.2 System Matrix (SM) Reconstruction Method

In the SM approach, the MPI signal received from a small source object located at a single voxel is recorded. Measurements are repeated as the source object is placed at each voxel within the FOV. These calibration measurements are used to construct the SM. The main experiment is conducted afterwards, and the MPI

signal is recorded for the actual object of interest. MPI image is finally reconstructed by solving an LSE comprising the SM and the signal measurements. The SM approach inherently accounts for field imperfections, and thus it has the potential to improve the reconstruction accuracy. At the same time, it requires the solution of a regularized inverse problem either via direct or iterative techniques, which are computationally demanding. ART is a technique of common choice due to its rapid convergence behavior [5, 22]. Recently, NFL has been proposed as an improved method for edge preservation [7].

2.2.2.1 Algebraic Reconstruction Technique (ART)

For the ART reconstruction, the following regularized least-squares problem is solved [5]:

$$\underset{\mathbf{c}}{\operatorname{argmin}} \left\|\mathbf{A}c - b\right\|_2^2 + \alpha \left\|c\right\|_2^2, \tag{2.17}$$

where $\mathbf{A}$ is the SM, $\mathbf{c}$ is the desired image to be reconstructed, c is the vectorized form of $\mathbf{c}$, b is the measurement vector, and α is a regularization constant.

In the ART method, at one iteration, the rows of $\mathbf{A}$ are swepth through while projecting the solution to the measurements as shown below [9]:

$$c_i = c_{i-1} + \frac{b(i) - < a_i^T,\ c_{i-1} >}{\left\|a_i\right\|_2^2} a_i^T, \text{ for } i = 1, ..., M, \tag{2.18}$$

where c_i is the reconstructed image at the i^{th} projection, $b(i)$ is the i^{th} element of the measurement vector, a_i is the i^{th} row of the SM, and M is the number of rows in $\mathbf{A}$. As seen in this relation, one iteration in ART corresponds to M inner iterations.

2.2.2.2 Nonnegative Fused LASSO (NFL)

In the NFL approach, the following problem is defined and solved [7]:

$$\underset{\mathbf{c}}{\operatorname{argmin}} \ \ \beta \left\|c\right\|_1 + \alpha TV_p(\mathbf{c}) + \frac{1}{2}\|\mathbf{A}c - b\|_2^2 + I_{pos}(c), \tag{2.19}$$

where β and α are regularization parameters, $I_{pos}(c)$ is the indicator function of all-positive elements such that its value is zero if all elements of $\mathbf{c} \geq 0$, and infinite if any element is negative, and $TV_p(c)$ is the TV term defined as [23]:

$$TV_p(\mathbf{c}) = \sum_{p=1}^{P} \sum_{(i,j)} w_p |\mathbf{c}_{(i,j)} - \mathbf{c}_{(i,j)+\mathcal{N}(p)}|. \tag{2.20}$$

Here, P is the number of directions. The directions and weights (w_p) for each direction is [24]:

$$\mathcal{N} = \big\{(1,0),(0,1),(1,1),(1,-1),(2,1),(2,-1),(1,2),(1,-2)\big\} \tag{2.21}$$

$$w_p = \begin{cases} \sqrt{5}-2, & p = 1,2 \\ \sqrt{5} - \frac{3}{2}\sqrt{2}, & p = 3,4 \\ \frac{1}{2}(1+\sqrt{2}-\sqrt{5}), & p = 5,6,7,8 \end{cases} \tag{2.22}$$

The taut string algorithm [25] is used to perform the TV minimization part of the problem defined in Eq. 2.19.

Chapter 3

Fast Image Reconstruction in MPI

This chapter is based on the publications titled "Comparison of System-Matrix-Based and Projection-Based Reconstructions for Field Free Line Magnetic Particle Imaging", Serhat Ilbey, Can Barış Top, Alper Güngör, Tolga Çukur, Emine Ulku Saritas, and H. Emre Güven, International Journal on Magnetic Particle Imaging, Vol. 3, No. 1., 1703022, 2017 (Reproduced with permission from Infinite Science Publishing, under a Creative Commons License.) and "Real-Time Three-Dimensional Image Reconstruction Using Alternating Direction Method of Multipliers for Magnetic Particle Imaging", Serhat Ilbey, Alper Güngör, Can Barış Top, Emine Ulku Saritas, and H. Emre Güven, Proc. of the 26^{th} Signal Processing and Communications Applications Conference, (SIU'18) İzmir, Turkey, 2018.

3.1 Introduction

The FFR in MPI systems typically spans a small spatial region of ellipsoidal shape, referred to as the FFP. This narrow FFP offers relatively increased spatial

resolution in MPI images. However, it also decreases the overall system sensitivity, as fewer nanoparticles can respond to the applied DF.

Creating an FFL instead of an FFP significantly increases the sensitivity of the MPI system [12]. To image a 3D volume with this approach, the FFL needs to be rotated and translated to sample the entire FOV. While this spatial positioning can be implemented mechanically [14, 26], electronic designs can be preferable in preclinical/clinical imaging setups to avoid mechanical positioning of the imaging system relative to the imaged subject. Recently, an electronically rotated FFL scanner was presented [15] based on an efficient coil design that enabled electronic rotation and translation of the FFL [27].

The data acquired along an FFL is essentially a projection of the MNP density along that line. This acquisition scheme bears close resemblance to that in Computerized Tomography (CT), where the acquired projection data can be written in the form of a Radon transform. Thus, x-space reconstruction for FFL MPI scans is based on the well-known projection reconstruction technique for CT images [13, 15, 28].

During x-space reconstruction, the MPI signal is first compensated for line velocity and particle relaxation, and deconvolved with the system's transfer function. The image can then be reconstructed using an inverse Radon transform [15]. In this x-space-based method [28], the magnetic field gradient is assumed to be independent of scan position and constant along the FFL. In addition, the FFL is assumed to be a straight line, although deviations can occur in practice [29–31].

This chapter compares the projection-based and SM reconstruction techniques for an FFL-MPI system, in terms of both reconstruction time and quality. For the SM reconstruction, this thesis proposes the use of ADMM algorithm, which is based on an augmented Lagrangian method [32]. The algorithm includes augmented Lagrangian terms that yield fast convergence speed. The SM based NFL algorithm is implemented, and the results are compared with the ADMM approach [16]. Moreover, ADMM is implemented on CUDA environment and real-time 3D image reconstruction results are presented on an NVIDIA®

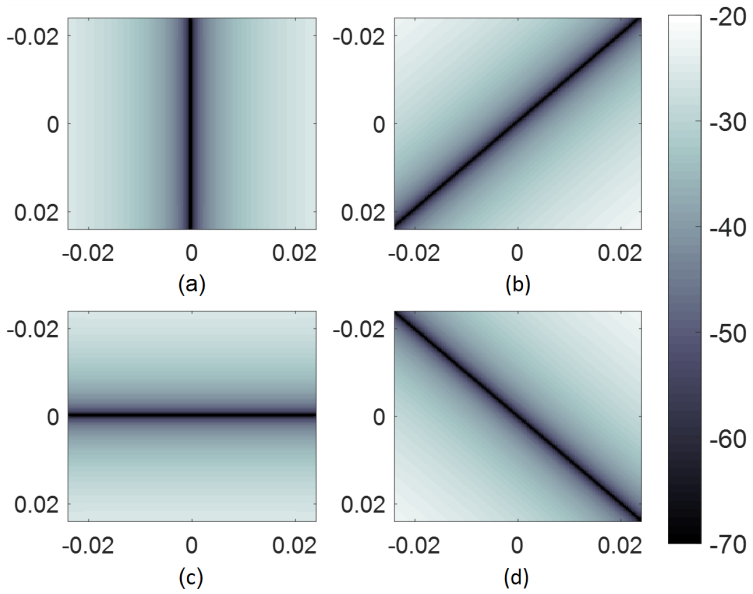

Figure 3.1: Selection field (dB) used in the simulations shown for (a) 0°, (b) 45°, (c) 90° and (d) 135° FFL angles. Horizontal axis: x (m), vertical axis: y (m).

GeForce® GTX 1080 GPU. The speed performance of these results were compared with those obtained with two CPUs.

3.2 Methods

An ideal FFL with an SF of 2 T/m was generated and scanned in a 48 mm x 48 mm FOV with a 25 kHz DF frequency (see Fig. 3.1). The pixel size used in the simulation was 300 μm x 300 μm. The FFL was rotated in 3° angular steps. A particle diameter of 25 nm was assumed [33, 34]. The transmit pulse width was 280 μs. A DF was applied to translate the FFL in the direction orthogonal to it. For simplicity, the DF was chosen as 60 mT, large enough to cover the entire FOV in a single cycle, releasing the need to adjust the amplitude offsets of the partial FOV images [6].

The MPI signal at each rotation angle θ_k ($k : 1, \ldots, \kappa$) was calculated using

the MPI signal equation [13]:

$$S(\theta_k, t) = -\frac{\partial}{\partial t} \int_{-\infty}^{\infty} \int_{-\infty}^{\infty} \mu_0 \mathbf{c}(x, y) \mathcal{L}(\beta |\mathbf{H}(x, y, t)| \frac{\mathbf{H}(x, y, t)}{|\mathbf{H}(x, y, t)|} \mathbf{q}_r dx dy, \tag{3.1}$$

where $\mathbf{c}(x, y)$ is the magnetic particle distribution inside the FOV. $\mathcal{L}$ is the Langevin function. $\beta = M_{sat}/\kappa_B T$, with M_{sat}: saturation magnetization $(0.6/\mu_0)$, κ_B : Boltzmann constant $(1.38\text{x}10^{-23})$, T: particle temperature (305 K). $\mathbf{q}_r$ denotes the sensitivities of the receiving coils, which are assumed to be uniform. $\mathbf{H}(x, y, t)$ is the total magnetic field at position (x, y) and time t.

To mimic realistic imaging conditions, the signal was convolved with an exponential relaxation kernel $r(t)$ with $\tau = 1\ \mu s$ [28,35], and additive white Gaussian noise (AWGN), $n(t)$, was added to the time domain signal with *awgn* function of MATLAB:

$$S_r(\theta_k, t) = S(\theta_k, t) * r(t) + n(t), \tag{3.2}$$

where

$$r(t) = \frac{1}{\tau} e^{-t/\tau} h(t), \tag{3.3}$$

with $\tau > 0$ is the relaxation time constant and $h(t)$ is the unit step function.

The received signal $S_r(\theta_k, t)$ was sampled at 10 MHz rate. A numerical binary vascular tree phantom (160 x 160 pixels) including three stenosis regions (see Fig. 3.2) was imaged using the presented FFL MPI configuration (see Fig. 3.1) with three different reconstruction methods.

Images of the vessel phantom were reconstructed using frequency components up to 1.25 MHz. As required in practice, to remove the direct feedthrough signal from the transmit coil, the frequency components up to and including the first harmonic were filtered out prior to reconstruction. All algorithms and the simulator were implemented on MATLAB, while chambolle projection step associated with TV is implemented using mex library of MATLAB in C, running on an Intel® Xeon® 2.4 GHz CPU 2620v3 12 cores, workstation (2 processors) with 64 GB RAM. The reconstructed images were compared with the reference image in terms of structural similarity index measure (SSIM) [36], and normalized root-mean-square error (nRMSE) for various SNR values (noise-free,

Figure 3.2: Numerical vessel phantom used in the simulations. Arrows show the regions with stenosis.

30 dB, 20 dB, and 10 dB), where noise power was calculated relative to the norm of the raw received time domain signal before filtering.

3.2.1 Image Reconstruction with SM Method

For the system calibration, the received signal's temporal Fourier transform data was stored for a known particle concentration at each pixel position for each rotation angle θ_k. These calibration data form the SM, $\mathbf{A}$. The temporal Fourier transform of the received signal in the imaging experiment was stored in the vector b. Then, the LSE $\mathbf{A}c = b$ was solved to reconstruct the vectorized particle distribution $\mathbf{c}$. Instead of using complex values in the equation system, the real and imaginary parts of $\mathbf{A}$ and b were separated and row-wise appended. Compared to complex operations that would yield 4-fold increased computational load, this real-valued formulation only poses a 2-fold increase, since the image of interest is real-valued.

For ADMM reconstruction, the problem was formulated as a constrained optimization minimizing the weighted sum of the TV and the l_1-norm of the image. Furthermore, a constraint on positivity of all elements of $\mathbf{c}$ was added. This constraint was implemented in the ADMM algorithm using an objective function $I_{pos}(c)$, which is the indicator function of all-positive elements such that its value is zero if all elements of $\mathbf{c} \geq 0$, and infinite if any element is negative. The

problem can therefore be expressed as:

$$\begin{aligned} \underset{\mathbf{c}}{\text{argmin}} \quad & \alpha_{l_1}\|\mathbf{c}\|_1 + \alpha_{TV}\mathrm{TV}(\mathbf{c}) + I_{pos}(\mathbf{c}) \\ \text{subject to} \quad & \|\mathbf{A}c - b\|_2 < \epsilon \end{aligned}, \tag{3.4}$$

where ϵ is the Euclidean norm of the presented noise, b is the received signal and TV is defined as:

$$\mathrm{TV}(\mathbf{c}) = \sum_{i,j} \sqrt{(\mathbf{c}_{i+1,j} - \mathbf{c}_{i,j})^2 + (\mathbf{c}_{i,j+1} - \mathbf{c}_{i,j})^2}. \tag{3.5}$$

Unlike [7], here an isotropic TV definition was used [37]. The data fidelity constraint in Eqn. 3.4 was also cast as a cost function such that the value of the indicator function is zero if the constraint is satisfied, and infinity otherwise. The resulting optimization problem was solved with the hybrid cost function presented in Eqn. 3.4, using ADMM [38].

ADMM solves a given problem by dividing it into smaller sub-problems. The pseudocode of the algorithm is given below, where μ is the step size. Here, $m = 2$ because a weighted sum of 2 cost functions are proposed as TV and l_1-norm.

Algorithm 1 ADMM with Hybrid Cost Function

Set iteration variable $n = 0$, choose step size $\mu > 0$
Initialize $\mathbf{z}_0^{(i)}$, $\mathbf{d}_0^{(i)}$
Repeat
$\hat{\mathbf{c}}_{n+1} = (m\mathbf{I} + \mathbf{A}^H\mathbf{A})^{-1}\left(\mathbf{A}^H(\mathbf{z}_n^{(0)} + \mathbf{d}_n^{(0)}) + \sum_{i=1}^{m}(\mathbf{z}_n^{(i)} + \mathbf{d}_n^{(i)})\right)$
$c_{n+1} = \hat{\mathbf{c}}_{n+1} \cdot (\hat{\mathbf{c}}_{n+1} > 0)$
for $i = 1, \cdots, m$ **do**
    $\mathbf{z}_{n+1}^{(i)} = \Psi_{\alpha_i\phi_i/\mu}\left(\mathbf{c}_{n+1} - \mathbf{d}_n^{(i)}\right)$
    $\mathbf{d}_{n+1}^{(i)} = \mathbf{d}_n^{(i)} + \mathbf{z}_{n+1}^{(i)} - \mathbf{c}_{n+1}$
end for
$\mathbf{z}_{n+1}^{(0)} = \Psi_{\mathbf{I}_{E(\epsilon,\mathbf{I},\mathbf{b})}}\left(\mathbf{A}\mathbf{c}_{n+1} - \mathbf{d}_n^{(0)}\right)$
$\mathbf{d}_{n+1}^{(0)} = \mathbf{d}_n^{(0)} + \mathbf{z}_{n+1}^{(0)} - \mathbf{A}\mathbf{c}_{n+1}$
$n \leftarrow n + 1$
Until some stopping criterion is satisfied.

Proximal mapping for TV with weighting α_{TV} is calculated using Chambolle

projections as in [39]. For the constraint function $\|\mathbf{A}c - b\|_2 \leq \epsilon$, proximal mapping is as follows:

$$\Psi_{\mathbf{I}_{E(\epsilon,\mathbf{I},\mathbf{b})}}(\mathbf{s}) = \begin{cases} \mathbf{s}, & \|\mathbf{s}-\mathbf{b}\|_2 \leq \epsilon \\ \mathbf{b} + \epsilon\frac{(\mathbf{s}-\mathbf{b})}{\|\mathbf{s}-\mathbf{b}\|_2}, & \|\mathbf{s}-\mathbf{b}\|_2 > \epsilon \end{cases} \tag{3.6}$$

where $\mathbf{I}_{E(\epsilon,\mathbf{I},\mathbf{b})}$ represents the indicator function of the feasible set $E(\epsilon, \mathbf{I}, \mathbf{b})$. Positivity constraint can be forced at the least squares step of the algorithm (see step 5, Alg. 1).

For comparison purposes, the NFL reconstruction was implemented on MATLAB using the previously presented algorithm in [7] (see Chapter 2.2.2.2 for details of NFL). It is worth mentioning that although the problem model stated for ADMM is very similar to the one in NFL, the TV formulations are different.

In ADMM solution, the ϵ value was scaled with the noise level. The ADMM parameters α_{l_1} and α_{TV}, and NFL parameters α and β were separately adjusted to attain the optimal SSIM values. ϵ, α, and β values used for each SNR value are given in Table 3.1.

As a stopping criterion for the above solutions,

$$\|\mathbf{c}_{n-1} - \mathbf{c}_n\|_2 / (\|\mathbf{c}_n\|_2 + 10^{-3}) < tol \tag{3.7}$$

was used, where n is the iteration number and tol was set as 10^{-5}. Maximum number of iterations was set to 5×10^3 for ADMM and 10^4 for NFL solutions. With these parameters, the SSIM values of the reconstructed images converged before reaching the maximum number of iterations or upon satisfying the stopping criterion.

For both ADMM and NFL solutions, regularized least squares solution of the problem was given as an initial solution to start the reconstruction algorithms.

Table 3.1: The parameters for ADMM and NFL that result in the best SSIM performance at each SNR value.

		Noise free	**30 dB**	**20 dB**	**10 dB**
ADMM	ϵ	0.1	0.68	2.14	6.74
	$\alpha_{\mathbf{l_1}}$	0.96	0.96	0.96	0.85
	$\alpha_{\mathbf{TV}}$	0.04	0.04	0.04	0.15
	μ	90	80	75	40
NFL	α	2×10^{-5}	2×10^{-5}	7×10^{-5}	7×10^{-4}
	β	9×10^{-4}	1×10^{-3}	6×10^{-4}	1×10^{-3}
	λ	1	1	1	1
	γ	1.8	1.8	1.8	1.8

3.2.2 Image Reconstruction with Projection-Based X-Space Method

The signal in the case of projection reconstruction imaging was previously given in Eqn. 2.14. Taking into account the nanoparticle relaxation effects, the received signal can be reformulated as follows:

$$S_r(\theta_k, t) = (D\Lambda'(t)(\hat{m}(v) * R(\mathbf{c})(\theta_k, \nu))) * r(t), \tag{3.8}$$

where $r(t)$ is the relaxation kernel [15, 35].

For the reconstruction process, the average of the DF cycles of the received signal was taken first, and the average signal was passed through a Wiener filter to remove the effect of relaxation. Then, the time domain signal was divided by the FFL velocity, and transformed to the spatial domain using interpolation. For interpolation, the *interp1* function of MATLAB was used with piece-wise cubic hermit interpolating polynomial (*pchip*). Next, the signal was deconvolved with the convolution kernel using a Wiener filter. This process was repeated for all rotation angles. Finally, the image was reconstructed with inverse Radon transform using the *iradon* function in MATLAB. Details of these reconstruction procedures were previously presented in [13, 15]. IRadon images can contain negative values as a side-effect of various filtering and deconvolution steps. These

values were set to zero, and images were then normalized to a maximum of one.

3.2.3 Real-Time 3D Image Reconstruction Using ADMM

In this thesis, real-time 3D image reconstruction is performed using the ADMM algorithm and its results are obtained by using a workstation having 1 NVIDIA® GeForce GTX 1080 GPU are presented [40]. The speeds of the reconstruction performance of ADMM using a GPU and CPUs are compared.

3.2.3.1 Simulation Parameters

The magnetic field gradients were set to 1.25 T/m, 1.25 T/m, and 2.5 T/m in the x-, y- and z-directions, respectively. The FOV was 20 mm x 20 mm x 10 mm, discretized into a 20 x 20 x 10 voxel grid. A Lissajous trajectory was used to scan the FFP at the entire FOV [21]. Maximum DF amplitude was 12.5 mT. The received signal was sampled at 20 MHz. 30 kHz - 1 MHz band of the signal was stored and used. *wgn* function of MATLAB was used to generate AWGN, which was added to the received signal. The MNPs were assumed to be mono-disperse with 25 nm diameter [33, 34]. The temperature of the system was set to 37 °C.

During the simulations, the numeric vessel object shown in Fig. 3.3a is used as a reference. In Fig. 3.4, the two-dimensional (2D) cross-sections of the same phantom are presented.

The ADMM algorithm is implemented in CUDA programming language. The time for the image reconstruction results obtained using a GPU were compared with those obtained using two CPUs.

The workstation used during the simulation had Intel® Xeon® CPU E5-2637 v4 @ 3.50 GHz (x2) CPUs, and 1 NVIDIA® GeForce GTX 1080 GPU and 256 GB RAM.

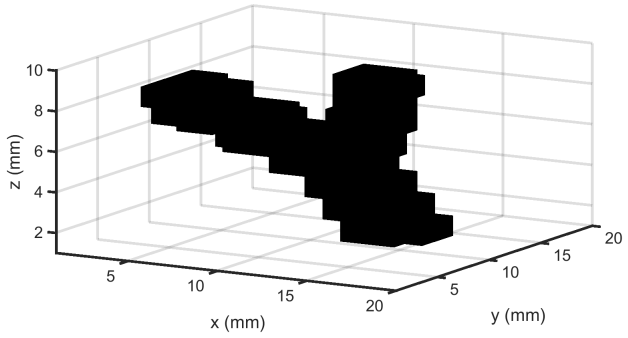

a)

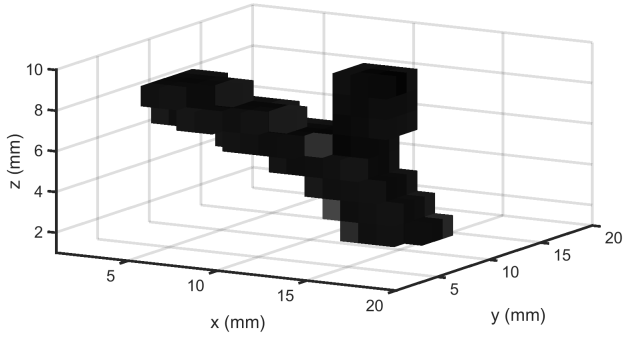

b)

Figure 3.3: **a)** The reference object and **b)** the reconstructed object in noise-free environment with 100 iterations of ADMM.

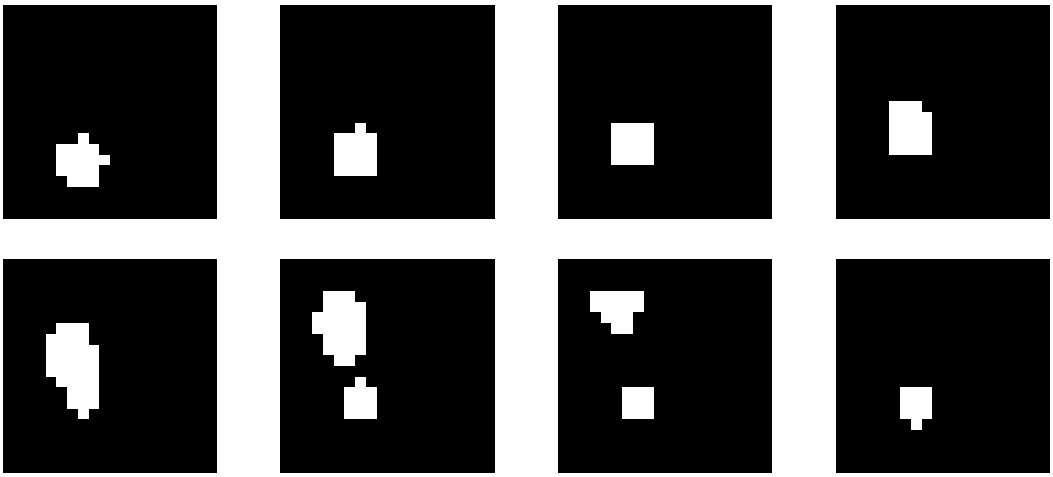

Figure 3.4: 2D cross-sections of the reference 3D object given in Fig. 3.3a. In this figure, the pixel intensity represents MNP concentration.

The image quality of the images were analyzed for different SNR levels (0 dB, 10 dB, 20 dB, ∞ dB) and number of iterations (5, 10, 100, 300).

3.2.4 Image Metrics

SSIM, Peak SNR (PSNR), and nRMSE metrics were used to quantitatively compare the reconstructed images. The SSIM [36] and PSNR metrics were calculated using the *ssim* and *psnr* functions in MATLAB with default input parameters. The nRMSE was calculated using the standard definition. All reconstructed images were normalized to a maximum of one prior to metric calculations.

3.3 Results

3.3.1 Comparison Results for SM-Based and Projection-Based Reconstruction Techniques

Figs. 3.5-3.8 show the SSIM and nRMSE results for the ADMM and NFL methods as a function of cumulative computation time, which is measured with *cputime* function in MATLAB, for noise-free case, 30 dB SNR, 20 dB SNR, and 10 dB SNR values. The corresponding images are given in Fig. 3.9. The SSIM and nRMSE parameters of the reconstructed images are tabulated for all noise levels in Table 3.2 and Table 3.3, respectively.

For the IRadon solution, the reconstruction time was 15.6 ms for all SNR values. Since this is a direct algorithm, its reconstruction time is significantly shorter and depends only on the size of the data.

For all noise levels, the images reconstructed with ADMM and NFL, and the resulting quality metrics (SSIM and nRMSE) are similar. Both system-matrix methods clearly depict vessel edges, yet the IRadon method yields blurry images

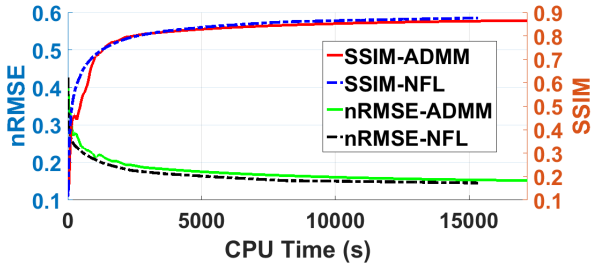

Figure 3.5: SSIM and nRMSE as a function of cumulative computation time for the noise-free case.

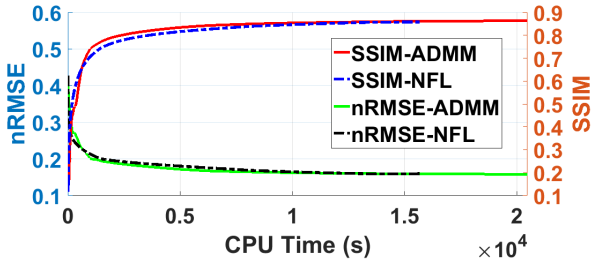

Figure 3.6: SSIM and nRMSE as a function of cumulative computation time at 30 dB SNR.

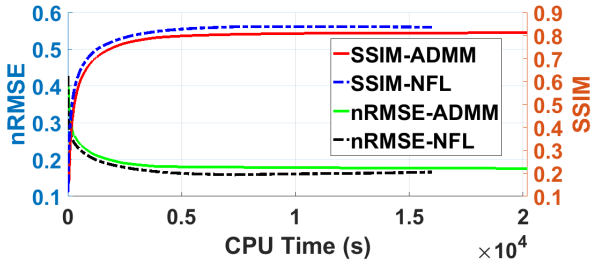

Figure 3.7: SSIM and nRMSE as a function of cumulative computation time at 20 dB SNR.

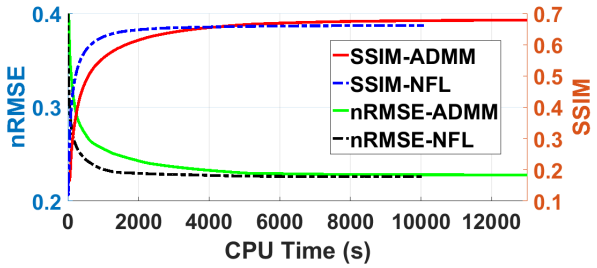

Figure 3.8: SSIM and nRMSE as a function of cumulative computation time at 10 dB SNR.

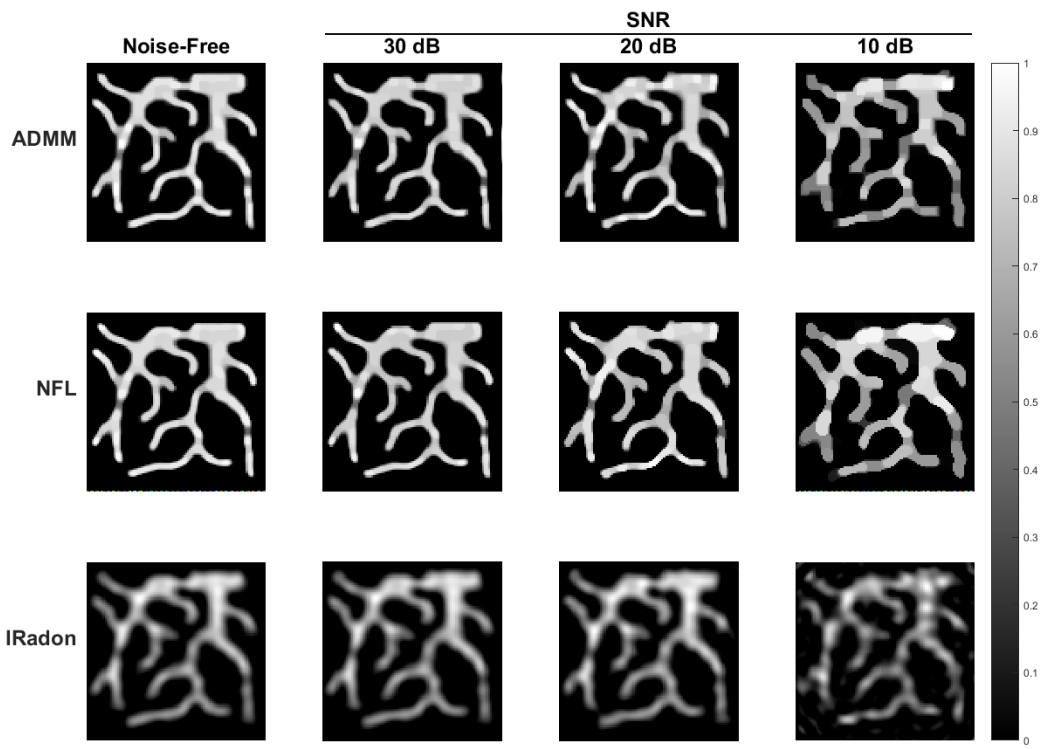

Figure 3.9: Final images of ADMM, NFL, and IRadon solutions for noise-free, 30 dB SNR, 20 dB SNR, and 10 dB SNR cases.

and lower SSIM values as shown in Fig. 3.9. Furthermore, gridding artifacts in IRadon reconstructions are visible at all SNR values and residual artifacts reach the intensity level of the vessels themselves at 10 dB. These residual artifacts result in a poor contrast in IRadon images compared to the system-matrix-based images.

In the presence of noise, ADMM and NFL show similar SSIM and nRMSE performance as a function of CPU time. For both methods, convergence is reached within similar total CPU time. These results are expected because ADMM and NFL use nearly identical problem formulations apart from the differences in the definitions of the TV term.

Table 3.2: SSIM of final images.

	Noise free	**30 dB**	**20 dB**	**10 dB**
ADMM	0.87	0.86	0.81	0.68
NFL	0.88	0.86	0.84	0.66
IRADON	0.55	0.55	0.54	0.42

Table 3.3: nRMSE of final images.

	Noise free	**30 dB**	**20 dB**	**10 dB**
ADMM	0.15	0.16	0.18	0.23
NFL	0.15	0.16	0.17	0.23
IRADON	0.27	0.27	0.27	0.30

3.3.2 Real-Time 3D Image Reconstruction Results Using ADMM

For each SNR level and different number of iterations, the vessel object is reconstructed. The reconstruction results for the noise-free case with 100 iterations are shown in Figs. 3.3b and 3.10.

For different SNR levels and number of iterations, the performance of the ADMM algorithm is measured and shown in Tables 3.4 and 3.5. Accordingly, the reconstruction quality increases with increasing SNR and number of iterations. Except for the infinite SNR case, which is not realistic, the PSNR and SSIM

Table 3.4: SSIM of the reconstructed object for each SNR level and iteration numbers.

SSIM	**Number of Iterations**			
SNR (dB)	**5**	**50**	**100**	**300**
∞	0.90	0.93	0.95	0.99
20	0.89	0.92	0.93	0.96
10	0.83	0.86	0.88	0.92
0	0.33	0.35	0.37	0.61

Table 3.5: PSNR of the reconstructed object for each SNR level and iteration numbers.

PSNR	**Number of Iterations**			
SNR (dB)	**5**	**50**	**100**	**300**
∞	22.0	28.7	30.4	41.5
20	21.9	24.4	24.7	25.5
10	21.2	22.7	22.9	23.3
0	17.9	18.8	18.9	18.7

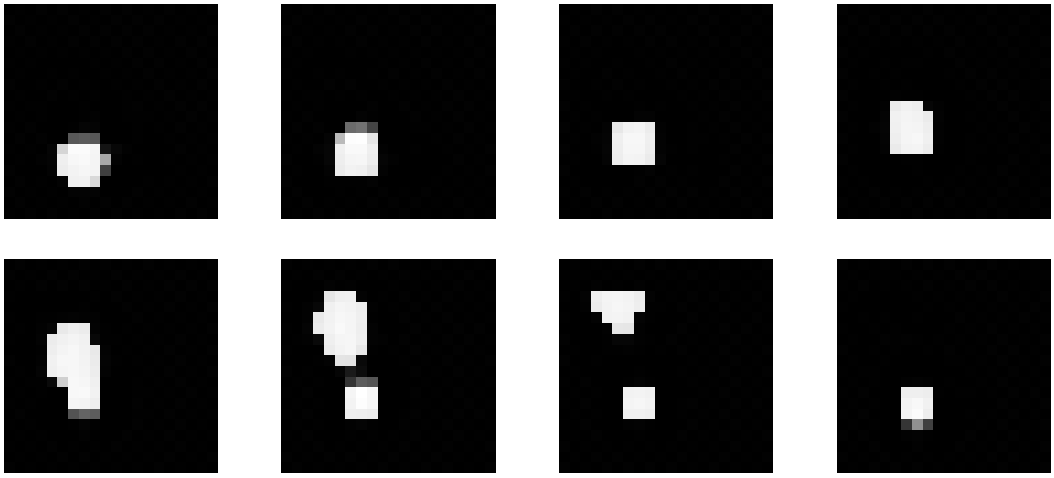

Figure 3.10: 2D cross-sections of the reconstructed object with 100 ADMM iterations, shown in Fig. 3.3b. In this figure, the pixel intensity represents the reconstructed MNP concentration.

values do not change significantly beyond 100 iterations.

In Table 3.6, the reconstruction time of the ADMM algorithm is presented. It is concluded that, for a 20 x 20 x 10 resolution system, for 100 iterations of ADMM, performing 8-9 volumetric reconstructions is possible using a single GPU. Moreover, the GPU performance was 30 to 65 times faster than the performance obtained with the CPUs.

Table 3.6: Processing time the reconstructed object for each SNR level and iteration numbers.

Number of Iterations	**5**	**50**	**100**	**300**
CPU duration (s)	0.25	2.33	4.73	14.10
GPU duration (s)	0.004	0.07	0.12	0.38
Acceleration Rate	62.5	33.3	39.4	37.1

3.4 Discussion

The SM-based ADMM and NFL methods outperformed the x-space-based IRadon method, which yielded blurry images, in terms of both SSIM and nRMSE. On the other hand, the IRadon method was very fast, resulting in reconstructions on the order of 10-20 ms. As the problem complexity of the ADMM and NFL solutions are similar, they converged to similar images.

While SSIM and nRMSE performance metrics are used commonly for image evaluation, purely quantitative inspections can be misleading without confirmation via visual inspection. In particular, SSIM and nRMSE are global metrics that do not reflect the type of reconstructions errors contained (e.g., blurring, noise, block artifacts). Further studies are needed to identify performance metrics that most highly correlate with the radiological evaluations in a clinical setting.

There were three small regions with stenosis included in the numerical phantom tested here. By means of visual inspection, it was observed that SM-based methods (ADMM and NFL) result in higher contrast near stenotic regions compared to projection-based (IRadon) reconstructions at all SNR values. In this study, the reconstruction parameters (α_{l_1} and α_{TV} vs. α and β) were selected freely to optimize the SSIM value in each method. Although the formulation of the SM solutions was similar for the ADMM and NFL approaches, the relative weightings assigned to l_1-norm and TV penalties were different. This is primarily due to the differences in the TV definitions. The TV definition in the NFL method was proposed by Chambolle [23], whereas the definition in ADMM was the isotropic TV [39]. Importantly, the isotropic TV term introduces a two-fold

scaling in magnitude that in turn roughly halves the relative TV penalty weights in ADMM.

In the simulations, the whole FOV was covered in a single scan, which required a relatively high DF amplitude and the use of large number of signal harmonics for high resolution. By dividing the FOV into smaller sections, the amplitude of the DF can be decreased and a smaller number of signal harmonics may suffice to obtain a similar resolution [41]. Utilizing a lower DF may actually be necessary to abide by the safety limits of the imaging procedure [42].

The simulations in this study were performed assuming ideal magnetic fields with a constant gradient and linear FFL. In non-ideal conditions, the gradient and the linearity of the FFL would deteriorate with increasing distance from the FOV center, depending on the coil system design. This non-ideality of the FFL results in signal fading and resolution losses [28]. If the FOV is defined as the region where the deviation of FFL gradient and linearity is within "acceptable limits", the results would be similar to the ideal-field conditions. The extent of the "acceptable limits" is out of the scope of this work and is a subject of future studies. The non-linearity of the FFL can be mitigated by using the measured fields in the reconstruction phase. This is already taken into account in the SM approach. For the projection-based reconstruction method, the formulation can be adapted for non-linear FFL paths. The decrease in the gradient amplitude may be a bigger concern as it directly affects the image resolution.

Although the reconstruction times compared to IRadon reconstruction are very high for SM-based ADMM and NFL algorithms, these algorithms can be parallelized to significantly improve their convergence time. GPUs may also be used for the same purpose, as these algorithms include many vector-based calculations. Furthermore, reducing SM size and system calibration procedure by applying CS techniques can also improve the convergence time of SM-based methods significantly [11, 43].

In the SM-based reconstruction methods, the regularized least squares solution of the problem was given as an initial condition. Performance may be

further improved by selecting the starting point as the image reconstructed by the fast IRadon method. A synergistic combination of the SM and projection-reconstruction methods that involves gridding steps followed by iterative reconstructions may improve the convergence speed and quality of the resulting images [44].

For a 20 x 20 x 10 resolution system, it is shown that performing 8-9 volumetric reconstructions per second is possible using a single GPU when the ADMM algorithm is used with 100 iterations.

Chapter 4

Fast Calibration Using Coded Calibration Scenes

4.1 Introduction

In MPI, the time needed for the system calibration procedure for a single calibration measurement is approximately 1.3 seconds [8]. Hence, even for a very small FOV with 20 x 20 x 20 voxels, a complete system calibration would take approximately 3 hours. In the literature, CS methods were proposed to mitigate the problem of long calibration scans [9–11, 22]. The motivation for using CS is that the SM can be represented very sparsely in Chebyshev domain, since its rows can be represented with Chebyshev polynomials of the second kind [22]. Moreover, it was shown that using the DCT or the discrete Fourier transform (DFT) domains as sparsifying domains is also sufficient to obtain a sparse SM representation [9].

SM reconstruction using the CS methods provided promising results using only 10%-20% of the full SM [10, 11]. However, these acceleration rates are still not sufficient for achieving acceptable calibration durations for the clinical MPI scanners. Recently, a hybrid calibration approach was proposed, in which the MNP sample is measured in a separate calibration device that emulates the magnetic

fields of the MPI system [8]. High SNR is achieved with this approach, enabling a faster calibration. However, this approach requires the magnetic fields to be known as a function of time for every voxel position.

In this chapter, the concept of "coded calibration scene" (CCS) is proposed for fast system calibration. In general, a CCS is defined as a calibration phantom that includes multiple number of MNP samples placed at random positions, with a size larger than or equal to the imaging FOV. One of the main advantages of the CCS appraoch is that the SNR is much higher than that of a single MNP sample measurement. Moreover, the received signal induced from the MNPs at multiple positions increases the information content of each calibration measurement [45]. Therefore, it is hypothesized that CCS-based calibrations can be done much faster when compared to the conventional calibration methods.

Using simulations, the performance of the proposed CCS approach is analyzed for different implementations considering its realization under practical imaging scenarios. ADMM was used to reconstruct the SM using CCS measurements [46]. It is shown that the proposed CCS approach provides significant improvements in image quality when compared to the standard CS method [10], even with highly accelerated calibrations. The effects of CCS filling rate, number of measurements, and SNR on the accuracy of the SM reconstruction are also investigated.

4.1.1 MPI System Calibration with Compressed Sensing

The imaging problem in MPI can be written as an LSE [1]:

$$\mathbf{A}c = b, \tag{4.1}$$

where $\mathbf{A}$ is the full SM, c is the vectorized representation of the MPI image to be reconstructed, b is the measurement vector including noise. Conventionally, the SM is obtained by measuring a single MNP sample at each voxel position in the FOV. The SM is sparse in DChT, DCT, and DFT domains, and the CS methods can be used to decrease the number of calibration measurements. In the standard CS method, an MNP sample is moved to randomly selected voxel

positions in the FOV grid, where the calibration data is taken. Then, the SM is reconstructed using convex optimization algorithms utilizing the sparsity property of the SM [10]. Accordingly, the following optimization problem is solved:

$$\begin{aligned} \underset{\mathbf{A}}{\text{argmin}} \quad & \left\|\mathbf{D}\mathbf{A}^T\right\|_1 \\ \text{subject to} \quad & \|\mathbf{A}\mathbf{C} - \mathbf{A_c}\|_F < \epsilon_c, \end{aligned} \tag{4.2}$$

where $\mathbf{D}$ is the DCT matrix, and $\mathbf{A_c}$ is the matrix of undersampled calibration measurements. $\mathbf{C}$ is the masking matrix that sifts the columns of A corresponding to the positions for which the calibration measurements are acquired. $\|\cdot\|_F$ is the Frobenius norm of a matrix and $\|\cdot\|_1$ is the sum of absolute values of all elements of a matrix.

4.1.2 Coded Calibration Scenes for System Calibration

In this chapter, the use of CCSs is proposed for the SM calibration. In the standard CS approach [10], each column of the $\mathbf{C}$ matrix in Eqn. 4.2 has only one non-zero entry (which is at the position of the MNP sample for the corresponding calibration measurement). On the other hand, in the proposed method, multiple number of MNP samples are present in each CCS. Therefore, each column of the $\mathbf{C}$ matrix corresponds to the nanoparticle distribution of a single CCS.

This chapter proposes five different approaches for practical implementation of CCS-based calibration, as described below:

4.1.2.1 Multi-CCS (M-CCS)

This is the basic implementation of the CCS [47]. Multiple number of CCSs are used for calibration. Each CCS has the size of the FOV. Voxel-sized MNP samples are randomly placed on the FOV grid with a certain filling rate. The filling rate is defined as the number of voxels with MNP samples divided by the total number of voxels. Examples of M-CCSs with different filling rates are shown in Fig. 4.1.

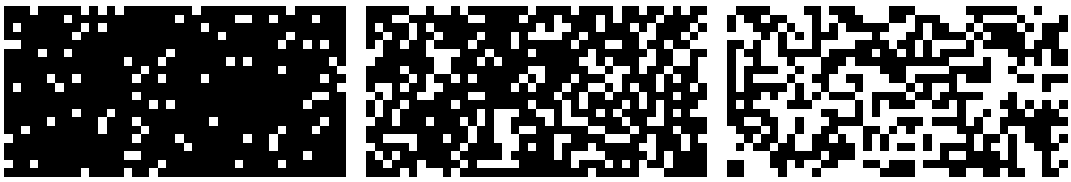

a) **b)** **c)**

Figure 4.1: Examples of the Multi-CCS (M-CCS) implementation that are randomly created with **a)** 10% **b)** 30% **c)** 50% filling rates. These CCSs have dimensions 20 mm x 10 mm with 40 x 20 pixels.

For calibration measurements, a CCS is placed in the FOV, measured, and then replaced by another CCS.

4.1.2.2 Sliding CCS (S-CCS)

This is an extended size CCS, which can be slided through the FOV. This way, the need for multiple CCS preparations and replacements are eliminated. An example of an S-CCS is shown in Fig. 4.2a. The S-CCS is slided in the y-direction by a predetermined number of grids before each calibration measurement.

4.1.2.3 Rotating CCS (R-CCS)

In the R-CCS case, a single CCS larger than the FOV size is rotated during the SM calibration measurements. An R-CCS example is shown in Fig. 4.2b. The size and position of the FOV are also depicted in the figure. The FOV is positioned as far away from the center of the R-CCS as possible, so that rotations cause maximal change in the MNP distribution that fall within the FOV.

4.1.2.4 Rotating and Sliding CCS (RS-CCS)

RS-CCS is a variation of the R-CCS implementation. Accordingly, the R-CCS is shifted after a full (360°) turn, and further measurements are taken at the

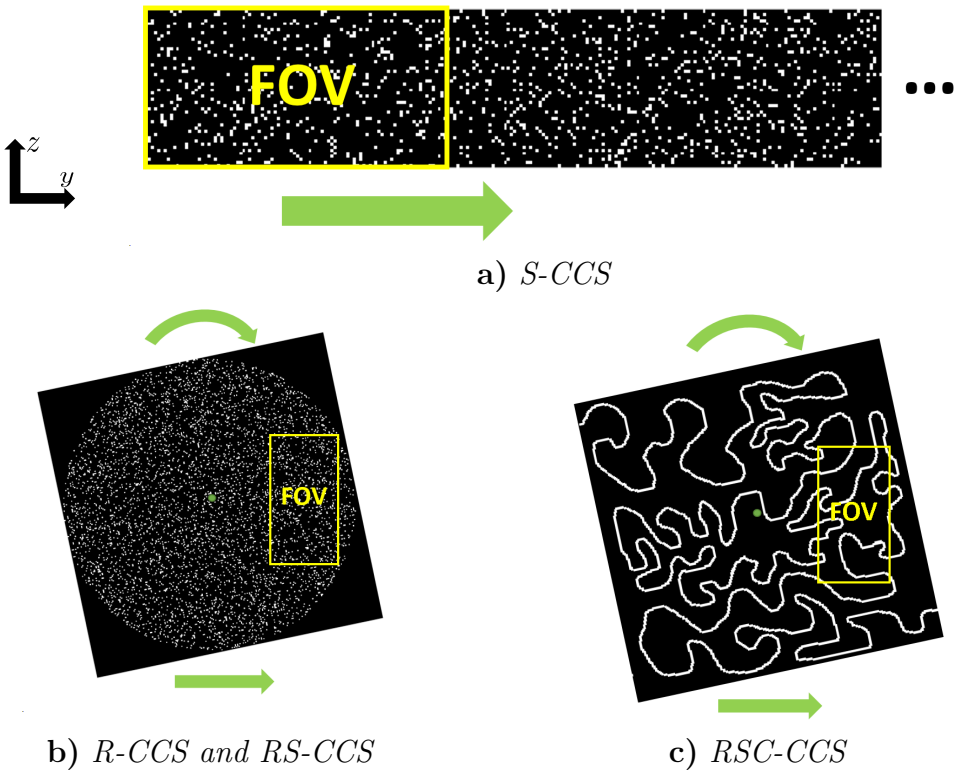

Figure 4.2: Different implementations of CCSs. **a)** Sliding CCS (S-CCS) filled randomly with MNPs and slided through the FOV. The length of the CCS is determined by the number of measurements and the amount of shift between two consecutive measurements. **b)** Rotating CCS (R-CCS) filled randomly with MNPs and rotated about its center. The R-CCS can be slided after a 360° turn, and rotated about a different axis, which is named as a Rotating and Sliding CCS (RS-CCS). **c)** Rotating and sliding connected CCS (RSC-CCS), where the MNPs are connectively distributed for a very practical implementation.

new rotation axis (Fig. 4.2b). The advantage of this implementation is that the calibration can be done using a smaller sized CCS compared to the S-CCS and R-CCS cases.

4.1.2.5 Rotating and Sliding Connected CCS (RSC-CCS)

This is a very practical implementation of an RS-CCS, in which the MNP samples are distributed in a connected fashion (Fig. 4.2c). This implementation allows filling (and emptying) the CCS with nanoparticles easily, e.g., by using a capillary tube filled with MNP solution.

There are a number of design parameters for the CCS implementations such as the filling rate, the number of measurements, the step size for the S-CCS case, and the step angle for the R-CCS and its variations. In the following sections, the effects of these parameters on the SM reconstruction performance are analyzed using simulations. The MPI images reconstructed using the SMs obtained by the different CCS implementations are also compared.

4.1.3 MPI Simulations

The proposed methods were evaluated using an in-house developed MPI simulator. The magnetic field gradients were set to 1.25 T/m and 2.5 T/m in the y- and z-directions, respectively. A Lissajous trajectory with 26.042 kHz and 25.252 kHz frequencies was used to scan the FFP at the entire FOV [21]. The MNPs were assumed to be mono-disperse with 25 nm diameter [33, 34]. The temperature of the system was set to 37 °C. Two different FOV sizes were used in the study. For the SM reconstruction performance analyses, the FOV was 20 mm x 10 mm, discretized into a 40 x 20 pixel grid. The corresponding DF amplitudes were 12.5 mT for both y- and z-directions. For the imaging analyses, a larger FOV with 50 mm x 25 mm (100 x 50 pixels) size was used with 31.25 mT DF amplitudes.

The received signal was calculated using the following equation [48]:

$$u(t) = \int_{FOV} -\mu_0 p^R(r) \cdot \frac{\partial \overline{m}(r,t)}{\partial t} \mathbf{c}(r) d^3 r, \tag{4.3}$$

where $\mathbf{c}$ is the MNP distribution in the FOV, p^R is the sensitivities of the receiver coils, which were assumed to be uniform, μ_0 is the free space magnetic permeability, and $\overline{m}$ is the average of the magnetic moment of the MNPs [48].

The received signal was sampled at 20 MHz. 30 kHz - 1 MHz band of the signal was stored and used. The built-in *wgn* function of MATLAB was used to generate AWGN, which was added to the received signal. The signal power obtained with a single MNP sample was used as the reference when calculating the standard deviation of the noise at different SNR levels.

The ratio of the number of measurements to the number of pixels in the FOV (N) is defined as the "measurement rate" and is denoted with the symbol δ. Accordingly, $\delta = 1$ corresponds to a full calibration with N measurements, whereas $\delta = 0.1$ corresponds to a calibration with only $N/10$ measurements.

4.1.4 System Matrix Reconstruction

To solve the problem defined in Eqn. 4.2, ADMM is used for both the standard CS and the proposed CCS approaches [46, 47]. In Fig. 4.3, the flowchart for the system calibration and system matrix reconstruction procedure is shown. For the standard CS case, each coded scene has only one MNP sample.

To assess the performance of the SM reconstruction quantitatively, the estimation error of the reconstructed SMs is calculated using normalized root mean squared error (nRMSE), defined as:

$$\text{nRMSE} = 20 \log_{10} \left(\frac{\sqrt{\frac{\sum_{i=1}^{M} \sum_{j=1}^{N} \left(\mathbf{A}_{ij} - \tilde{\mathbf{A}}_{ij} \right)^2}{MN}}}{\sigma_{\tilde{\mathbf{A}}}} \right), \tag{4.4}$$

where M and N are the number of rows and columns of $\mathbf{A}$, respectively. $\tilde{\mathbf{A}}$ is

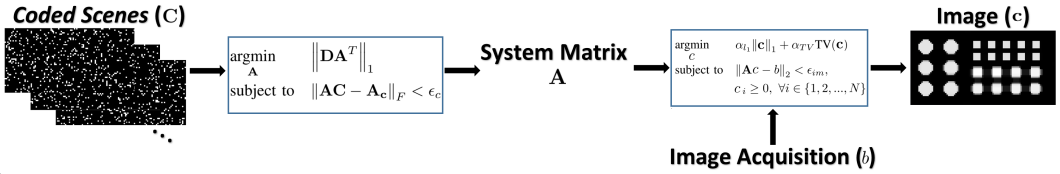

Figure 4.3: The flowchart for CCS-based MPI system calibration and image reconstruction. The calibration measurements ($\mathbf{A_c}$) are taken using the CCSs (represented as C in the problem formulations). First, the full system matrix ($\mathbf{A}$) is estimated with these measurements using ADMM, by minimizing the l_1-norm of the DCT of the SM subject to the data fidelity constraint. Next, the image acquisition starts. With the estimated $\mathbf{A}$ and imaging measurements b, the MPI image is reconstructed using ADMM by minimizing the weighted sum of TV and l_1-norm of the reconstructed image with a data fidelity and nonnegativity constraint.

the ideal system matrix obtained with a full calibration measurement and $\sigma_{\tilde{\mathbf{A}}}$ is the standard deviation of the elements of $\tilde{\mathbf{A}}$.

Monte Carlo (MC) simulations were run until convergence of the mean and variance for each CCS analysis. 200 MC simulations were sufficient to reach convergence for all the analysis.

4.1.5 Image Reconstruction

For the image reconstruction, the following problem was solved with ADMM [16]:

$$\begin{aligned} \underset{\mathbf{c}}{\text{argmin}} \quad & \alpha_{l_1}\|\mathbf{c}\|_1 + \alpha_{TV}\text{TV}(\mathbf{c}) \\ \text{subject to} \quad & \|\mathbf{A}c - b\|_2 < \epsilon_{im} \\ & c_i \geq 0,\ \forall i \in \{1,2,...,N\} \end{aligned} \quad , \tag{4.5}$$

where $\mathbf{c}$ is the unknown 2D image, c is vectorized representation of $\mathbf{c}$, and c_i is the i^{th} position of c. This problem was defined in a way that a weighted sum of the TV and the l_1-norm of the reconstructed images is minimized. Moreover, a nonnegativity constraint was inserted to the problem definition, as the MNP density can not be negative [16, 17]. Defining the problem with TV and l_1-norm cost functions is highly suitable for MPI, since MPI images are sparse

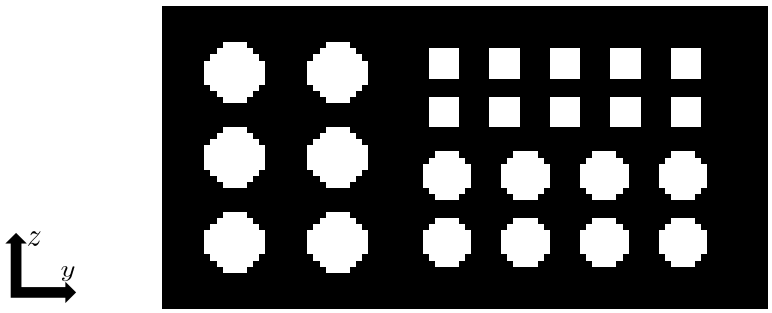

Figure 4.4: Numerical phantom used in the simulations. The disks have 5 mm (left) and 4 mm (right, bottom) diameter. The squares (right, top) have 2.5 mm side length.

and block-wise contiguous. For example, the images of blood vessels have these properties naturally.

The schematic describing the image reconstruction is presented in Fig. 4.3 for the M-CCS case. The numerical phantom used in the study is shown in Fig. 4.4. There are disk objects that have 4 mm and 5 mm diameters and squares whose side length is 2.5 mm. This phantom was used to analyze the image reconstruction performance in terms of resolution.

For quantitative comparison of the resultant images, SSIM [36] and PSNR values were calculated using the built-in *ssim* and *psnr* functions of MATLAB with the default parameters.

4.2 Results

4.2.1 Effects of filling rate, measurement rate, and SNR

For the M-CCS case, the effect of the filling rate on the SM reconstruction was analyzed for different measurement rates (δ = 0.5, 0.2, 0.1, and 0.05) and for various SNR levels (0 dB, 10 dB, 20 dB, 30 dB, and ∞) with MC simulations. The contour plots of the SM reconstruction nRMSE values are shown in Fig. 4.5. The simulated filling rates were $1/800$, 0.1, 0.3, 0.5, 0.7, 0.9, and $799/800$. Note that

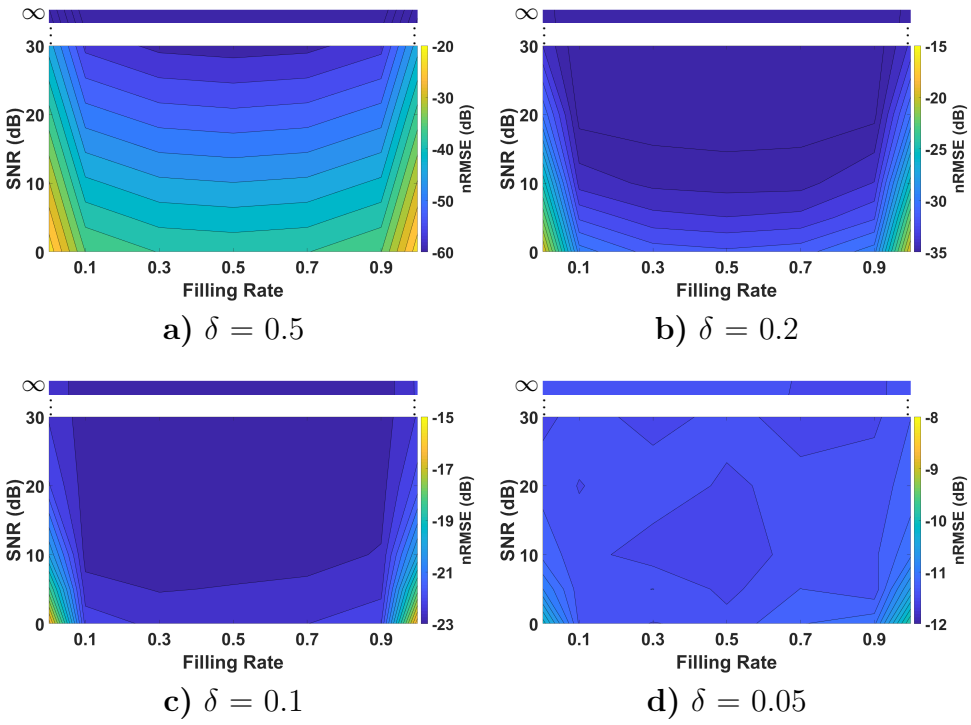

Figure 4.5: Contour plots of the nRMSE of the estimated system matrices for different filling rates and δ's for the M-CCS case. For the filling rates, the following values were used: $^{1}/_{800}$, 0.1, 0.3, 0.5, 0.7, 0.9, and $^{799}/_{800}$.

$^{1}/_{800}$ filling rate corresponds to a CCS with a single-voxel MNP sample, which is equivalent to the standard CS method. The dual case is $^{799}/_{800}$ filling rate, in which all voxels except for one voxel are filled with MNP samples. In addition, cross sections of these plots for 10 dB SNR are presented in Fig. 4.6a.

The results show that for $\delta = 0.5$ and $\delta = 0.2$, the best filling rate is 0.5, independent of the SNR level. At lower measurement rates of $\delta = 0.1$ and $\delta = 0.05$, the effect of the filling rate is gradually reduced, as better seen in Fig. 4.6a. At $\delta = 0.1$, while the best filling rate is 0.3, the filling rates between 0.1-0.9 also have comparable performances. At $\delta = 0.05$, the contour plot in Fig. 4.5d is not monotonous along the vertical direction due to both the reduced effect of the filling rate and the high standard deviation of the MC simulations (see error bars in Fig. 4.6a). For the optimal filling rates at 10 dB SNR, nRMSE is improved by 15 dB, 10 dB, 3 dB, and 0.5 dB compared to the standard CS case (i.e., a filling rate of $^{1}/_{800}$) for $\delta = 0.5$, 0.2, 0.1, and 0.05, respectively (Fig. 4.6a). As seen in

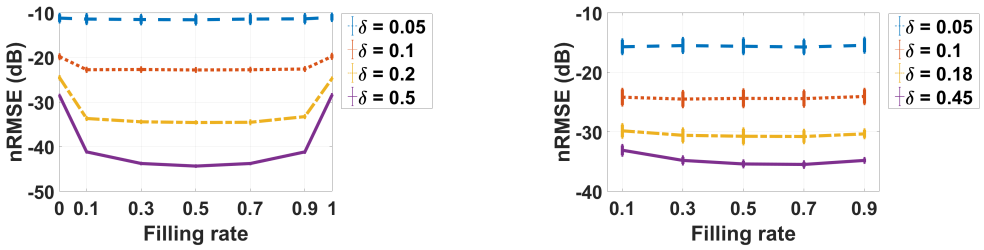

a) *M-CCS* **b)** *R-CCS*

Figure 4.6: The nRMSE (dB) as a function of filling rate for $\delta = 0.2$ at 0.1 filling rate and 10 dB SNR for **a)** M-CCS and **b)** R-CCS. The mean values and standard deviations across repeated Monte Carlo simulations are plotted.

Fig. 4.5, for all four measurement rates, choosing the correct filling rate causes even more significant improvements in nRMSE if the SNR is lower than 10 dB.

A similar analysis was also done for the full rotation of the R-CCS case at 0.45, 0.18, 0.1, and 0.05 measurement rates, corresponding to 1°, 2.5°, 4.5°, and 9° angle-steps, respectively. The size of the R-CCS was 50 mm x 50 mm (corresponding to 100 x 100 voxels), and the distance between the FOV center and the rotation center was 17.5 mm in these simulations. The contour plots of the SM reconstruction nRMSE values are shown in Fig. 4.7 for filling rates of 0.1, 0.3, 0.5, 0.7, and 0.9. In addition, cross sections of these plots for 10 dB SNR are presented in Fig. 4.6b.

For the $\delta = 0.45$ case the best filling rate is 0.7, whereas for $\delta = 0.18$, it is 0.5. Similar to the M-CCS case, the effect of the filling rate is reduced at lower measurement rates (see Fig. 4.6b). At $\delta = 0.1$, filling rates between 0.3-0.7 have similar performances. At delta = 0.05, the filling rate has almost no effect on the SM reconstruction performance, causing the contour plot to be dominated by the standard deviation of the MC simulations.

4.2.2 Effects of Sliding Step Size and Angle Step Size

For the S-CCS case, the effect of the sliding step size was analyzed from 1 to 40 grid step size, for $\delta = 0.2$ at 0.1 filling rate and 10 dB SNR. Note that for

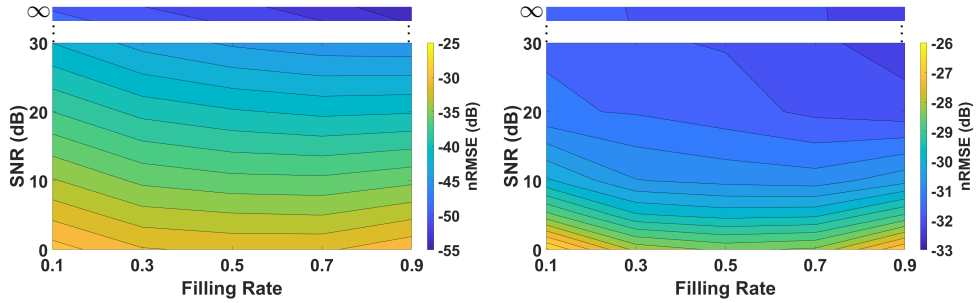

a) $\delta = 0.45$ (Angle step: 1°) **b)** $\delta = 0.18$ (Angle step: 2.5°)

c) $\delta = 0.1$ (Angle step: 4.5°) **d)** $\delta = 0.05$ (Angle step: 9°)

Figure 4.7: Contour plots of the nRMSE of the estimated system matrices for different filling rates and δ's for the R-CCS case. For the filling rates, the following values were used: 0.1, 0.3, 0.5, 0.7, and 0.9.

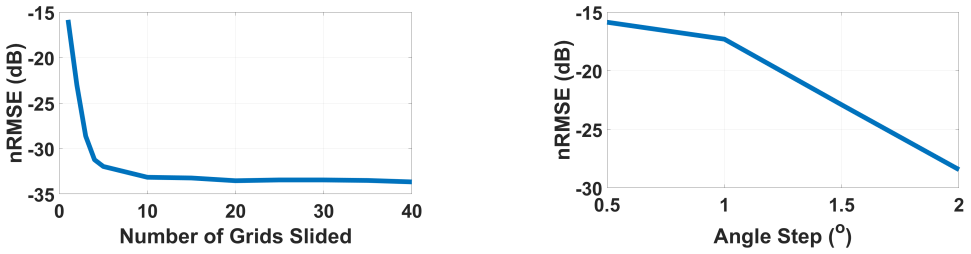

a) *S-CCS* **b)** *R-CCS*

Figure 4.8: The nRMSE (dB) as a function of **a)** the number of slided grids for S-CCS, and **b)** the angle step for R-CCS before each measurement with parameters: 0.1 filling rate, $\delta = 0.2$, and 10 dB SNR.

the FOV size of 40 x 20 voxels, the total number of calibration measurements at $\delta = 0.2$ is 160. Sliding along the y-direction with one-grid step size before each measurement requires an S-CCS with a total length of 199 grids. On the other hand, using a 40-grid step size corresponds to fully replacing the effective CCS before each measurement (i.e., equivalent to M-CCS), and requires an S-CCS with a length of 6400 grids. As shown in Fig. 4.8a, the nRMSE for SM reconstruction decays sharply from one to four grid steps, emphasizing the need for a sufficient level of variation among the effective regions of the S-CCS that fall within the FOV. On the other hand, a similar performance is observed when step size is increased from 10 to 40 grids.

For the R-CCS case, the effect of angle step size was analyzed between 0.5° to 2° step for $\delta = 0.2$ at 0.1 filling rate and 10 dB SNR. With the total number of calibration measurements fixed to 160, the total rotation range of the R-CCS increases from 80° to 320° when the angle step size is increased from 0.5° to 2°. The resulting nRMSE for SM reconstruction as a function of rotation angle step size is shown in Fig. 4.8b. Accordingly, increasing the angle step size increases the performance significantly, once again emphasizing the need for variation among effective portions of the R-CCS.

4.2.3 Performance Under a Limited Calibration Time

For a limited system calibration duration, a question is how many different CCSs should be measured for optimal performance for a given measurement SNR and duration. In this study, the trade-off of using the time budget to increase the SNR (via averaging) vs. to vary the effective CCS was analyzed.

For the S-CCS with 40-grid step size (i.e., equivalent of M-CCS) case, it was assumed that the time required for sliding between two consecutive measurements is one second, measurement time for a single Lissajous cycle is one millisecond, SNR is -30 dB, filling rate is 0.1, and the total calibration time is $\sim$320 seconds. When the number of calibration measurements is reduced, then the time

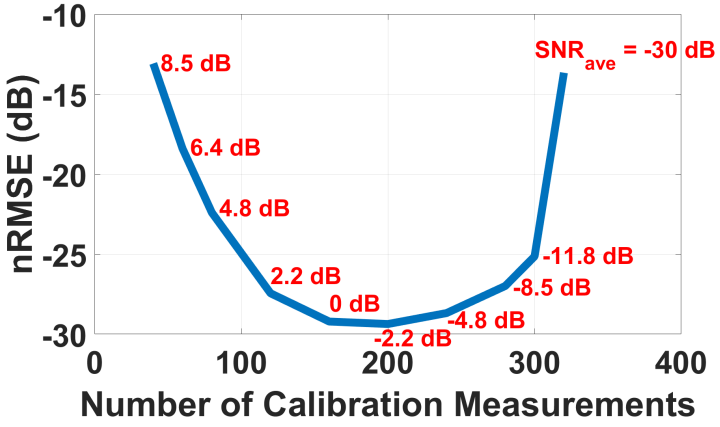

a) S-CCS with 40-grid step size

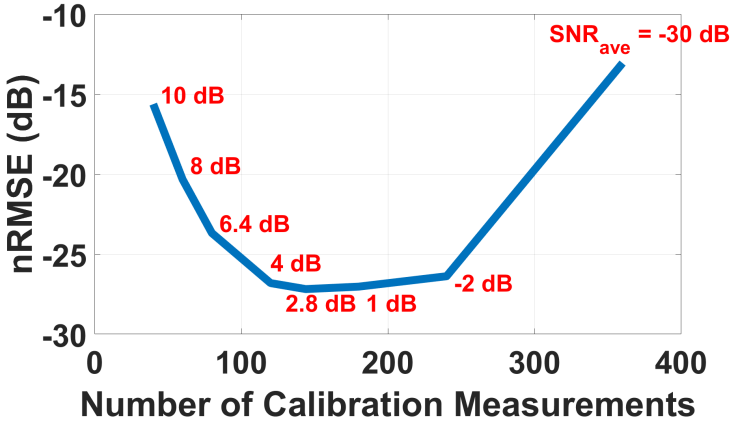

b) *R-CCS*

Figure 4.9: The nRMSE as a function of **a)** the total number of measurements for S-CCS case and **b)** R-CCS case used in the calibration measurements with 0.1 filling rate.

allocated for each measurement is increased. For instance, when 160 calibration measurements are taken instead of 320, then the allocated time for each measurement time becomes 2 seconds instead of 1 ms. So, for each calibration measurement, 2000 Lissajous cycles are performed. Then, the SNR after the averaging (SNR_{ave}) increases by $10\log_{10}(2000/160) = 30$ dB, so that SNR_{ave} becomes 0 dB (see Fig. 4.9a). The nRMSE and the corresponding SNR levels as a function of number of calibration measurements are given in Fig. 4.9a. For the system parameters used, taking 200 measurements (i.e., $\delta = 0.25$) is optimal.

Similar results are obtained for the R-CCS case (Fig. 4.9b), for 360 seconds total calibration time, -30 dB SNR, and 0.1 filling rate. Between each consecutive measurements, the time needed was assumed to be 1 second. The rotation angle-step was set according to the number of calibration measurements. For example, for 144 measurements, the angle-step was 2.5°. The optimal number of measurements is 144 for this case, corresponding to $\delta = 0.18$.

4.2.4 Image Reconstruction Results

The images reconstructed using the resultant SMs of standard CS, M-CCS, S-CCS, RS-CCS, and RSC-CCS methods are presented in Fig. 4.10 for the phantom in Fig. 4.4 with a FOV size of 100 x 50 voxels. Three different scenarios were tested: $\delta = 0.2$ and SNR = 10 dB, $\delta = 0.2$ and SNR = 0 dB, and $\delta = 0.1$ and SNR = 0 dB. For all cases, the filling rate of the CCSs was 0.1. For the S-CCS case, the sliding step size was 5 grids in the z-direction. For the RS-CCS and RSC-CCS cases, the distance between the center of the FOV and the rotation center was 45 mm in the z-direction, and the angle step size was 1°. After each full turn, the CCS was slided 30 grids in the z-direction twice for the $\delta = 0.2$ case. This corresponds to 1080 measurements ($\delta = 0.216$) in total with three full turns of the CCS. On the other hand, for $\delta = 0.1$ case, 1.5° angle-steps was used and the CCS was slided once for 40 grids in the z-direction. This corresponds to 480 measurements ($\delta = 0.096$) in total with two full turns of the CCS.

For all scenarios in Fig. 4.10, the CCS methods outperform the standard CS

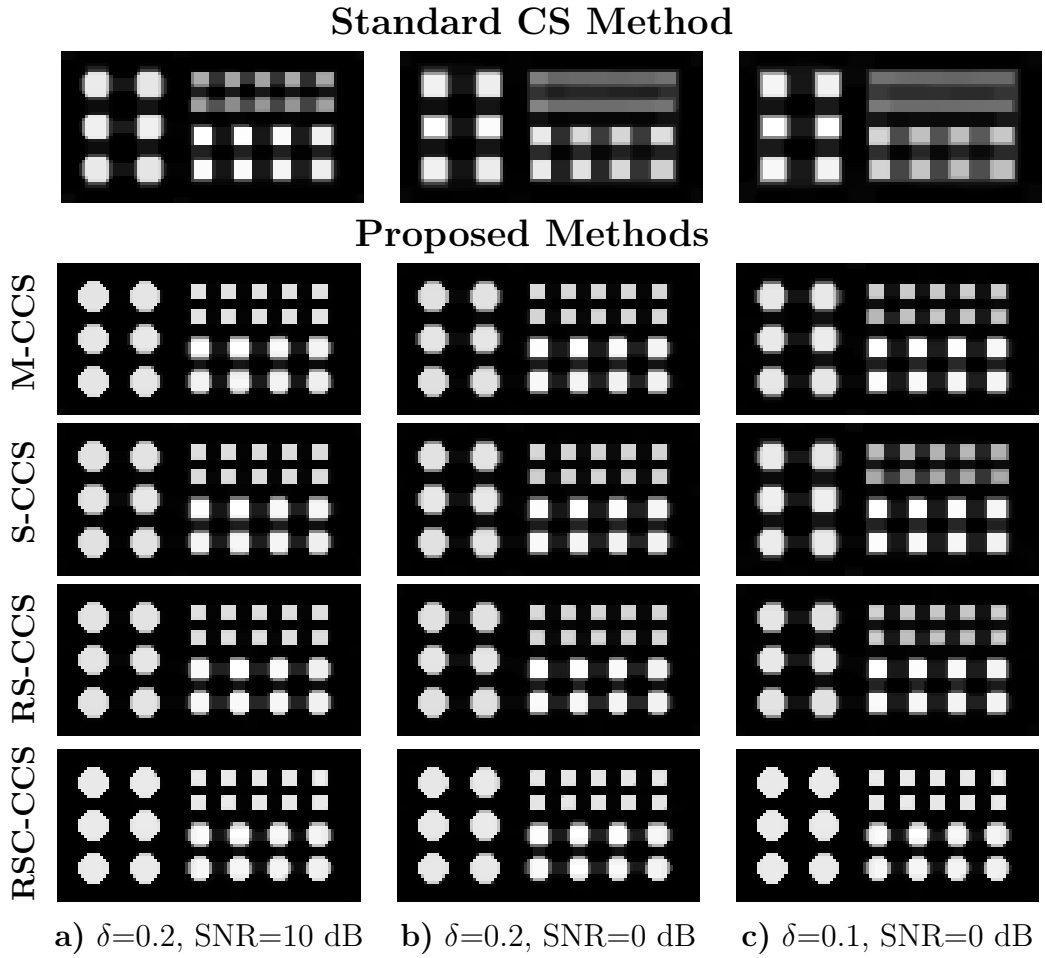

Figure 4.10: Reconstructed images with system matrices reconstructed via M-CCS, RS-CCS, RSC-CCS, S-CCS (with 5 grid sliding step) types of CCSs, for **a)** $\delta = 0.2$ and 10 dB SNR, **b)** $\delta = 0.2$ and 0 dB SNR, and **c)** $\delta = 0.1$ and 0 dB SNR scenarios. The filling rate of the CCSs were 0.1.

Table 4.1: SSIM of the reconstructed images for different δ and SNR values with the standard CS and the CCS approaches. The filling rate of CCSs were 0.1. SNR values are given in dB.

Methods	***δ=0.2, SNR=10***	***δ=0.2, SNR=0***	***δ=0.1, SNR=0***
Standard CS	0.71	0.55	0.49
M-CCS	0.94	0.88	0.81
S-CCS	0.91	0.86	0.74
RS-CCS	0.93	0.89	0.83
RSC-CCS	0.97	0.95	0.91

Table 4.2: PSNR of the reconstructed images for different δ and SNR values with the standard CS and the CCS approaches. The filling rate of CCSs were 0.1. SNR and PSNR values are given in dB.

Methods	***δ=0.2, SNR=10***	***δ=0.2, SNR=0***	***δ=0.1, SNR=0***
Standard CS	13.64	12.04	11.63
M-CCS	19.72	16.94	15.26
S-CCS	18.00	16.28	14.16
RS-CCS	18.84	17.16	15.42
RSC-CCS	22.68	20.19	17.62

method, which is evident by both visual inspection and quantitative results given in Tables 4.1 and 4.2. The small square objects in the top right of the numerical phantom were successfully resolved by the CCS based reconstructions, whereas they could not be resolved with the standard CS method. Although the randomness of the CCS is partially violated for the RSC-CCS case, the reconstructed images have the highest quality.

For the S-CCS case, the effect of sliding step size on the reconstructed images was also analyzed, for the cases of 1, 5, and 10 grid step sizes. The results are shown in Fig. 4.11 for $\delta = 0.2$ and SNR = 10 dB, and filling rate = 0.1. Sliding 5 to 10 grids in the y-direction after each measurement resulted in almost identical image quality, whereas sliding one grid yielded a significantly worse image. This result is consistent with the SM reconstruction analysis in Fig. 4.8a,

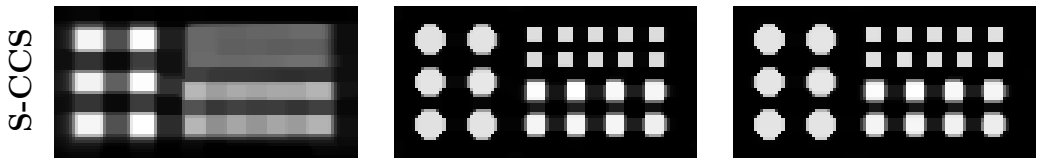

a) *1 grid step* **b)** *5 grid step* **c)** *10 grid step*

Figure 4.11: Image reconstruction results for the S-CCS with **a)** *1 grid sliding step*, **b)** *5 grid sliding step*, and **c)** *10 grid sliding step*. $\delta = 0.2$, SNR = 10 dB, and filling rate = 0.1.

and highlights the fact that the effective CCS needs to vary among measurements to ensure that each measurement provides maximal amount of new information.

4.3 Discussion

The results of the simulations on the imaging performance showed that significantly improved image quality is obtained with the proposed CCS methods compared to the standard CS method for the same SNR and measurement rate. This is a consequence of (i) the higher SNR of the CCS compared to single MNP measurements, and (ii) the higher amount of information gathered from a single measurement. The filling rate analyses showed that the optimal filling rate is between 0.3 and 0.7. While SNR increases with increasing filling rates above 0.5, the coherency of the measurements also increase, limiting the SM reconstruction performance. The symmetrical behavior with respect to the filling rate shows that the reconstruction performance is limited by the ill-posedness of the problem, rather than the measurement noise. Furthermore, the effect of the measurement noise on the SM reconstruction error decreases with decreasing measurement rates.

The CCS method is based on measuring multiple "scenes" with randomly positioned MNPs, which is the M-CCS case. Other CCS variations were proposed looking from a practical implementation point of view. The MNP samples are placed at random positions in these CCSs (S-CCS and R-CCS), but during the sliding and rotation movements, the successive measurements become correlated. Hence, the randomness and incoherence of measurements, which is a necessary

condition in CS, is partially violated. On the other hand, the sparsity level of the SM is sufficiently high that these variations are feasible. For example, sliding a long CCS for 4 or 5 grids before each measurement was enough to get sufficient level of incoherency among measurements for a 40-grid FOV and a measurement rate of 0.2. Although this is an advantage of the S-CCS, a large CCS with at least 20 times the size of FOV is required, which may not be practical.

The main advantage of the CCS is that it may be possible to obtain calibration data during a continuous movement of the CCS, since the measurement SNR is not a concern. If this is the case, calibration duration can be significantly reduced compared to the conventional SM calibration methods. To this end, the position of CCS should be known precisely to generate the calibration mask matrix. The position of the moving CCS can be tracked by precision position measurement devices such as laser trackers, if necessary.

If the measurement SNR is relatively low, the number of averaging and the measurement rate can be optimized. For a continuous CCS movement, the speed of the motion should be adjusted accordingly.

The R-CCS implementations can be used to mitigate the large size requirements of the S-CCS. By using rotation and translation, the measurements can be diversified. Using only the rotation movement resulted in higher SM reconstruction errors compared to the M-CCS case for the R-CCS size used in this study (i.e., with a size 10 times the FOV area). However, the RS-CCS case resulted in a similar imaging performance as the M- and S-CCS cases with only 2-3 rotation centers.

In case the CCS is implemented as a mold that can be filled with MNP samples, filling and emptying the random CCS pattern with MNP samples may be impractical. Here, a connected CCS pattern is proposed as a solution. To minimize the size, it is implemented as a RS-CCS. The imaging results show that this implementation has the highest image quality among all proposed implementations of CCSs. This may be caused by slightly higher filling rate of this implementation (0.12 vs. 0.1 for other CCS cases).

Chapter 5

Conclusion

In this thesis, three main contributions are presented for system calibration and image reconstruction in MPI.

Firstly, the SM and x-space-based reconstruction methods for MPI are comparatively analyzed. ADMM is proposed as a fast SM method in MPI. The x-space method is computationally fast compared to the SM methods and it does not require a time-consuming system calibration scan [11, 43]. The reconstruction time for the x-space method was 10-20 ms whereas it was about 10 minutes for the SM-based methods. However, x-space reconstructions can yield residual artifacts and relatively low contrast. The results show that SM methods outperform the x-space method in terms of SSIM and nRMSE metrics that reflect enhanced image contrast and artifact suppression. For example, for 20-dB SNR level, the image reconstructed with the ADMM algorithm has 0.18 nRMSE value and 0.81 SSIM value, whereas the one reconstructed with the IRadon method has 0.27 nRMSE value and 0.54 SSIM value.

Secondly, 8-9 volumetric reconstructions for a 20 x 20 x 10 resolution system are performed using a single GPU with the ADMM algorithm. The GPU performance is shown to be approximately 40 times faster than the performance obtained with the CPUs.

Finally, a fast calibration method is proposed for SM using CCSs and CS. Its different variations are demonstrated considering practical implementation. The results show that system calibration using CCSs outperforms the standard CS SM reconstruction, which uses a single MNP sample. The quality of the reconstructed images significantly increases for the same number of measurements and SNR level. For example, when the calibration measurements are reduced by a factor of 5 at 10-dB SNR, the standard CS method has 13.64 dB PSNR value and 0.71 SSIM value, whereas the proposed CCS approach has 22.68 dB PNSR value and 0.97 SSIM value.

The techniques proposed in this thesis substantially reduce the required number of measurements for the system calibration, and significantly improve the MPI image reconstruction process in terms of both the reconstruction speed and the resulting image quality.

Bibliography

[1] B. Gleich and J. Weizenecker, "Tomographic imaging using the nonlinear response of magnetic particles," *Nature*, vol. 435, no. 7046, pp. 1214–1217, 2005.

[2] E. Saritas, P. Goodwill, L. Croft, J. Konkle, K. Lu, B. Zheng, and S. Conolly, "Magnetic Particle Imaging MPI for NMR and MRI researchers," *J. Magn. Reson.*, vol. 229, pp. 116–126, 2013.

[3] J. Weizenecker, B. Gleich, and J. Borgert, "A simulation study on the resolution and sensitivity of magnetic particle imaging," *Phys. Med. Biol.*, vol. 52, no. 21, pp. 6363–6374, 2007.

[4] T. Knopp, S. Biederer, T. Sattel, M. Erbe, and T. Buzug, "Prediction of the Spatial Resolution of Magnetic Particle Imaging Using the Modulation Transfer Function of the Imaging Process," *IEEE Trans. Med. Imag.*, vol. 30, no. 6, pp. 1284–1292, 2011.

[5] T. Knopp, J. Rahmer, T. Sattel, S. Biederer, J. Weizenecker, B. Gleich, J. Borgert, and T. Buzug, "Weighted iterative reconstruction for magnetic particle imaging," *Phys. Med. Biol.*, vol. 55, no. 6, pp. 1577–1589, 2010.

[6] P. W. Goodwill and S. M. Conolly, "Multidimensional X-Space Magnetic Particle Imaging," *IEEE Trans. Med. Imag.*, vol. 30, no. 9, pp. 1581–1590, 2011.

[7] M. Storath, C. Brandt, M. Hofmann, T. Knopp, J. Salamon, A. Weber, and A. Weinmann, "Edge Preserving and Noise Reducing Reconstruction

for Magnetic Particle Imaging," *IEEE Trans. Med. Imag.*, vol. 36, no. 1, pp. 74–85, 2017.

[8] A. von Gladiss, M. Graeser, P. Szwargulski, T. Knopp, and T. M. Buzug, "Hybrid system calibration for multidimensional magnetic particle imaging," *Phys. Med. Biol.*, vol. 62, no. 9, p. 3392, 2017.

[9] J. Lampe, C. Bassoy, J. Rahmer, J. Weizenecker, H. Voss, B. Gleich, and J. Borgert, "Fast reconstruction in magnetic particle imaging," *Phys Med Biol*, vol. 57, no. 4, pp. 1113–1134, 2012.

[10] T. Knopp and A. Weber, "Sparse Reconstruction of the Magnetic Particle Imaging System Matrix," *IEEE Trans. Med. Imag.*, vol. 32, no. 8, pp. 1473–1480, 2013.

[11] A. Weber and T. Knopp, "Reconstruction of the Magnetic Particle Imaging System Matrix Using Symmetries and Compressed Sensing," *Adv. Math. Phys.*, vol. 2015, p. 460496, 2015.

[12] J. Weizenecker, B. Gleich, and J. Borgert, "Magnetic particle imaging using a field free line," *J. Phys. D: Appl. Phys.*, vol. 41, no. 10, p. 105009, 2008.

[13] T. Knopp, M. Erbe, T. Sattel, S. Biederer, and T. Buzug, "A Fourier slice theorem for magnetic particle imaging using a field-free line," *Inverse Probl.*, vol. 27, no. 9, p. 095004, 2011.

[14] J. J. Konkle, P. W. Goodwill, O. M. Carrasco-Zevallos, and S. M. Conolly, "Projection reconstruction magnetic particle imaging," *IEEE transactions on medical imaging*, vol. 32, no. 2, pp. 338–347, 2013.

[15] K. Bente, M. Weber, M. Graeser, T. Sattel, M. Erbe, and T. Buzug, "Electronic field free line rotation and relaxation deconvolution in magnetic particle imaging," *IEEE Trans. Med. Imag.*, vol. 34, no. 2, pp. 644–651, 2015.

[16] S. Ilbey, C. B. Top, A. Güngör, T. Çukur, E. U. Saritas, and H. E. Güven, "Comparison of system-matrix-based and projection-based reconstructions for field free line magnetic particle imaging," *International Journal on Magnetic Particle Imaging*, vol. 3, no. 1, 2017.

[17] S. Ilbey, C. B. Top, T. Çukur, E. U. Saritas, and H. E. Güven, "Image reconstruction for magnetic partical imaging using an augmented lagrangian method," in *International Symposium on Biomedical Imaging*, 2017.

[18] S. Boyd, "Distributed Optimization and Statistical Learning via the Alternating Direction Method of Multipliers," *Foundations and Trends® in Machine Learning*, vol. 3, no. 1, pp. 1–122, 2011.

[19] S. Ilbey, C. B. Top, A. Güngör, T. Çukur, E. U. Saritas, and H. E. Güven, "Fast system calibration with sliding and rotating coded calibration scenes for magnetic particle imaging," *IEEE Trans. Med. Imag.*, 2018, (Under Preperation).

[20] P. Goodwill and S. Conolly, "The x-Space Formulation of the Magnetic Particle Imaging process: One-Dimensional Signal, Resolution, Bandwidth, SNR, SAR, and Magnetostimulation," *IEEE Trans. Med. Imag.*, vol. 29, no. 11, pp. 1851–1859, 2010.

[21] T. Knopp, S. Biederer, T. Sattel, J. Weizenecker, B. Gleich, J. Borgert, and T. Buzug, "Trajectory analysis for magnetic particle imaging," *Phys. Med. Biol.*, vol. 54, no. 2, pp. 385–397, 2009.

[22] J. Rahmer, J. Weizenecker, B. Gleich, and J. Borgert, "Signal encoding in magnetic particle imaging: properties of the system function," *BMC Medical Imaging*, vol. 9, no. 4, 2009.

[23] A. Chambolle, "Finite-differences discretizations of the mumford-shah functional," *Esaim Math. Model. Numer. Anal.*, vol. 33, no. 2, pp. 261–288, 1999.

[24] M. Storath, A. Weinmann, J. Frikel, and M. Unser, "Joint image reconstruction and segmentation using the Potts model," *Inverse Probl.*, vol. 31, no. 2, p. 025003, 2015.

[25] L. Condat, "A Direct Algorithm for 1-D Total Variation Denoising," *IEEE Signal Process. Lett.*, vol. 20, no. 11, pp. 1054–1057, 2013.

[26] K. Murase, S. Hiratsuka, R. Song, and Y. Takeuchi, "Development of a system for magnetic particle imaging using neodymium magnets and gradiometer," *Jpn. J. Appl. Phys.*, vol. 53, no. 6, p. 067001, 2014.

[27] T. Knopp, M. Erbe, S. Biederer, T. Sattel, and T. Buzug, "Efficient generation of a magnetic field-free line," *Med. Phys.*, vol. 37, no. 7, pp. 3538–3540, 2010.

[28] P. Goodwill, J. Konkle, B. Zheng, E. Saritas, and S. Conolly, "Projection X-Space Magnetic Particle Imaging," *IEEE Trans. Med. Imag.*, vol. 31, no. 5, pp. 1076–1085, 2012.

[29] J. Konkle, P. Goodwill, O. Carrasco-Zevallos, and S. Conolly, "Projection Reconstruction Magnetic Particle Imaging," *IEEE Trans. Med. Imag.*, vol. 32, no. 2, pp. 338–347, 2012.

[30] M. Erbe, T. Knopp, T. Sattel, and T. Buzug, "Influence of Magnetic Field Optimization on Image Quality Achieved for Efficient Radon-Based Reconstruction in Field Free Line Imaging in MPI," in *Springer Proceedings in Physics*, vol. 140, pp. 225–229, 2012.

[31] H. Medimagh, P. Weissert, G. Bringout, K. Bente, M. Weber, K. Gräfe, A. Cordes, and T. Buzug, "Artifacts in field free line magnetic particle imaging in the presence of inhomogeneous and nonlinear magnetic fields," *Curr. Dir. Biomed. Eng.*, vol. 1, no. 1, pp. 245–248, 2015.

[32] H. E. Güven, A. Güngör, and M. Çetin, "An augmented lagrangian method for complex-valued compressed sar imaging," *IEEE Transactions on Computational Imaging*, vol. 2, no. 3, pp. 235–250, 2016.

[33] R. Ferguson, A. Khandhar, S. Kemp, H. Arami, E. Saritas, L. Croft, J. Konkle, P. Goodwill, A. Halkola, J. Rahmer, J. Borgert, S. Conolly, and K. Krishnan, "Magnetic Particle Imaging With Tailored Iron Oxide Nanoparticle Tracers," *IEEE Trans. Med. Imag.*, vol. 34, no. 5, pp. 1077–1084, 2015.

[34] A. P. Khandhar, P. Keselman, S. J. Kemp, R. M. Ferguson, P. W. Goodwill, S. M. Conolly, and K. M. Krishnan, "Evaluation of peg-coated iron oxide

nanoparticles as blood pool tracers for preclinical magnetic particle imaging," *Nanoscale*, vol. 9, pp. 1299–1306, 2017.

[35] L. Croft, P. Goodwill, and S. Conolly, "Relaxation in X-Space Magnetic Particle Imaging," *IEEE Trans. Med. Imag.*, vol. 31, no. 12, pp. 2335–2342, 2012.

[36] Z. Wang, A. C. Bovik, H. R. Sheikh, and E. P. Simoncelli, "Image quality assessment: from error visibility to structural similarity," *IEEE Transactions on Image Processing*, vol. 13, pp. 600–612, April 2004.

[37] L. Rudin, S. Osher, and E. Fatemi, "Nonlinear total variation based noise removal algorithms," *Physica D*, vol. 60, no. 1, pp. 259–268, 1992.

[38] H. Güven, A. Güngör, and M. Cetin, "An Augmented Lagrangian Method for Complex-Valued Compressed SAR Imaging," *IEEE Trans. Comput. Imaging*, vol. 2, no. 3, pp. 235–250, 2016.

[39] A. Chambolle, "Total Variation Minimization and a Class of Binary MRF Models," in *International Workshop on Energy Minimization Methods in Computer Vision and Pattern Recognition*, pp. 136–152, 2005.

[40] S. Ilbey, A. Güngör, C. B. Top, E. U. Saritas, and H. E. Güven, "Real-time three-dimensional image reconstruction using alternating direction method of multipliers for magnetic particle imaging," in *Signal Processing and Communications Applications Conference, İzmir, Turkey*, IEEE, 2018.

[41] L. Croft, P. Goodwill, J. Konkle, H. Arami, D. Price, A. Li, E. Saritas, and S. Conolly, "Low drive field amplitude for improved image resolution in magnetic particle imaging," *Med. Phys.*, vol. 43, no. 1, pp. 424–435, 2016.

[42] E. U. Saritas, P. W. Goodwill, G. Z. Zhang, and S. M. Conolly, "Magnetostimulation Limits in Magnetic Particle Imaging," *IEEE Trans. Med. Imag.*, vol. 32, no. 9, pp. 1600–1610, 2013.

[43] A. von Gladiss, M. Ahlborg, T. Knopp, and T. Buzug, "Compressed Sensing of the System Matrix and Sparse Reconstruction of the Particle Concentration in Magnetic Particle Imaging," *IEEE Trans. Magn.*, vol. 51, no. 2, p. 6501304, 2015.

[44] P. Vogel, T. Kampf, M. Rückert, and V. Behr, "Flexible and Dynamic Patch Reconstruction for Traveling Wave Magnetic Particle Imaging," *Intern. J. Magnetic Particle Imaging*, vol. 2, no. 2, p. 1611001, 2016.

[45] G. Arce, D. Brady, L. Carin, H. Arguello, and D. Kittle, "Compressive Coded Aperture Spectral Imaging," *IEEE Signal Processing Magazine*, vol. 31, no. 1, pp. 105–115, 2014.

[46] S. Ilbey, C. B. Top, E. U. Saritas, and H. E. Güven, "Fast system calibration for mpi using a rotating coded calibration scene," in *8th International Workshop on Magnetic Particle Imaging (IWMPI)*, 2018.

[47] S. Ilbey, A. Güngör, C. B. Top, E. U. Saritas, and H. E. Güven, "Coded scenes for fast system calibration in magnetic particle imaging," in *International Symposium on Biomedical Imaging*, IEEE, 2018.

[48] T. Knopp and T. M. Buzug, *Magnetic Particle Imaging: An Introduction to Imaging Principles and Scanner Instrumentation.* Berlin/Heidelberg: Springer, 2012.